DOI: 10.1016/j.mattod.2021.05.006
FERMILAB-PUB-21-775-SQMS

Making the Most of your Electrons: Challenges and Opportunities in Characterizing Hybrid Interfaces with STEM

Stephanie M. Ribet,[†,‡] Akshay A. Murthy,[†,‡,¶] Eric W. Roth,[§] Roberto dos Reis,[‡,§] and Vinayak P. Dravid[*,‡,¶,§]

† *These authors contributed equally*

‡ *Department of Materials Science and Engineering, Northwestern University, Evanston, IL*

¶ *International Institute of Nanotechnology, Northwestern University, Evanston, IL*

§ *The NUANCE Center, Northwestern University, Evanston, IL*

E-mail: v-dravid@northwestern.edu

Abstract

Inspired by the unique architectures composed of hard and soft materials in natural and biological systems, synthetic hybrid structures and associated soft-hard interfaces have recently evoked significant interest. Soft matter is typically dominated by fluctuations even at room temperature, while hard matter (which often serves as the substrate or anchor for the soft component) is governed by rigid mechanical behavior. This dichotomy offers considerable opportunities to leverage the disparate properties offered by these components across a wide spectrum spanning from basic science to engineering insights with significant technological overtones. Such hybrid structures, which include polymer nanocomposites, DNA functionalized nanoparticle superlattices and metal organic frameworks to name a few, have delivered promising insights into the areas of catalysis, environmental remediation, optoelectronics, medicine, and beyond.

This manuscript has been authored by Fermi Research Alliance, LLC under Contract No. DE-AC02-07CH11359 with the U.S. Department of Energy, Office of Science, Office of High Energy Physics.

The interfacial structure between these hard and soft phases exists across a variety of length scales and often strongly influence the functionality of hybrid systems. While scanning/transmission electron microscopy (S/TEM) has proven to be a valuable tool for acquiring intricate molecular and nanoscale details of these interfaces, the unusual nature of hybrid composites presents a suite of challenges that make assessing or establishing the classical structure-property relationships especially difficult. These include challenges associated with preparing electron-transparent samples and obtaining sufficient contrast to resolve the interface between dissimilar materials given the dose sensitivity of soft materials.

We discuss each of these challenges and supplement a review of recent developments in the field with additional experimental investigations and simulations to present solutions for attaining a nano or atomic-level understanding of these interfaces. These solutions present a host of opportunities for investigating and understanding the role interfaces play in this unique class of functional materials.

1 Introduction

The unusual hierarchical architectures composed of hard and soft materials in natural and biological systems has inspired a surge in interest related to the synthesis of hybrid nanostructures. These hard/soft interfaces (HSI) are ubiquitous across multiple length-scales (down to the molecular scale) in nature and play a critical role in ensuring favorable properties under a variety of environmental conditions. For instance, bones are composed hard hydroxyapatite and soft collagen in order to provide the necessary structural support to protect internal organs.[1,2] Similar interfaces in teeth between hard enamel and soft dentin provide the extraordinary mechanical strength and toughness that teeth display.[3–5] These types of interfaces are also found in the case of nacre, or mother of pearl, which exhibits excellent mechanical strength and resilience in part due to the underlying architecture composed of hard aragonite and soft biopolymer.[6,7]

In traditional materials science, the composite structure approach has been leveraged for successfully improving properties of structural materials. Hard, brittle materials can be made tougher and more resilient by introducing softer fibrous or particulate species into the underlying matrix.[8,9] More recently a similar approach has been deployed at the nanoscale. Examples include functionalized nanoparticles,[10,11] DNA-mediated nanoparticle superlattices,[12,13] 0D/2D nanocomposites,[14] and metal-organic framework - nanoparticle composites.[15–17] These hybrid materials have numerous applications including in supercapacitors,[18] flame retardants,[19] catalysis,[20,21] environmental remediation,[22] optoelectronics,[23,24] batteries,[25] photovoltaic cells,[26] medicine,[11,14] and wearable technologies.[27]

1.1 Hard/Soft Interfaces (HSI): Structure dictates performance

Although there is great diversity in these materials and their applications, they are unified in the fact that many of their exceptional and exotic phenomena arise from the bridging of two dissimilar materials. This unusual HSI region can consist of an abrupt interface or a slowly graded interphase. Examples of abrupt soft/hard interfaces include 0D/2D core-shell architectures.[24] In this case, the hard nanoparticle core and soft layered shell interface can be atomically sharp and devoid of any buffer region. The types of bonds present at these HSI dictate the level of charge and photocarrier injection present as well as the magnitude of the diffuse interface scattering that phonons face during heat dissipation.[28]

Alternatively, polymer nanocomposites are examples of systems that demonstrate gradually evolving interfacial regions, or interphases separating the hard and soft components. In this area, which can extend on the order of hundreds of nanometers, the soft polymer undergoes chemical and physical changes near the hard material inclusion.[29–31] In this case, atomic and molecular-scale structures provide information regarding the nature of the chemical bonds present between different constituent materials. This information thus helps explain the level of load transfer and stress concentrations that arise when these materials undergo deformation processes.[32]

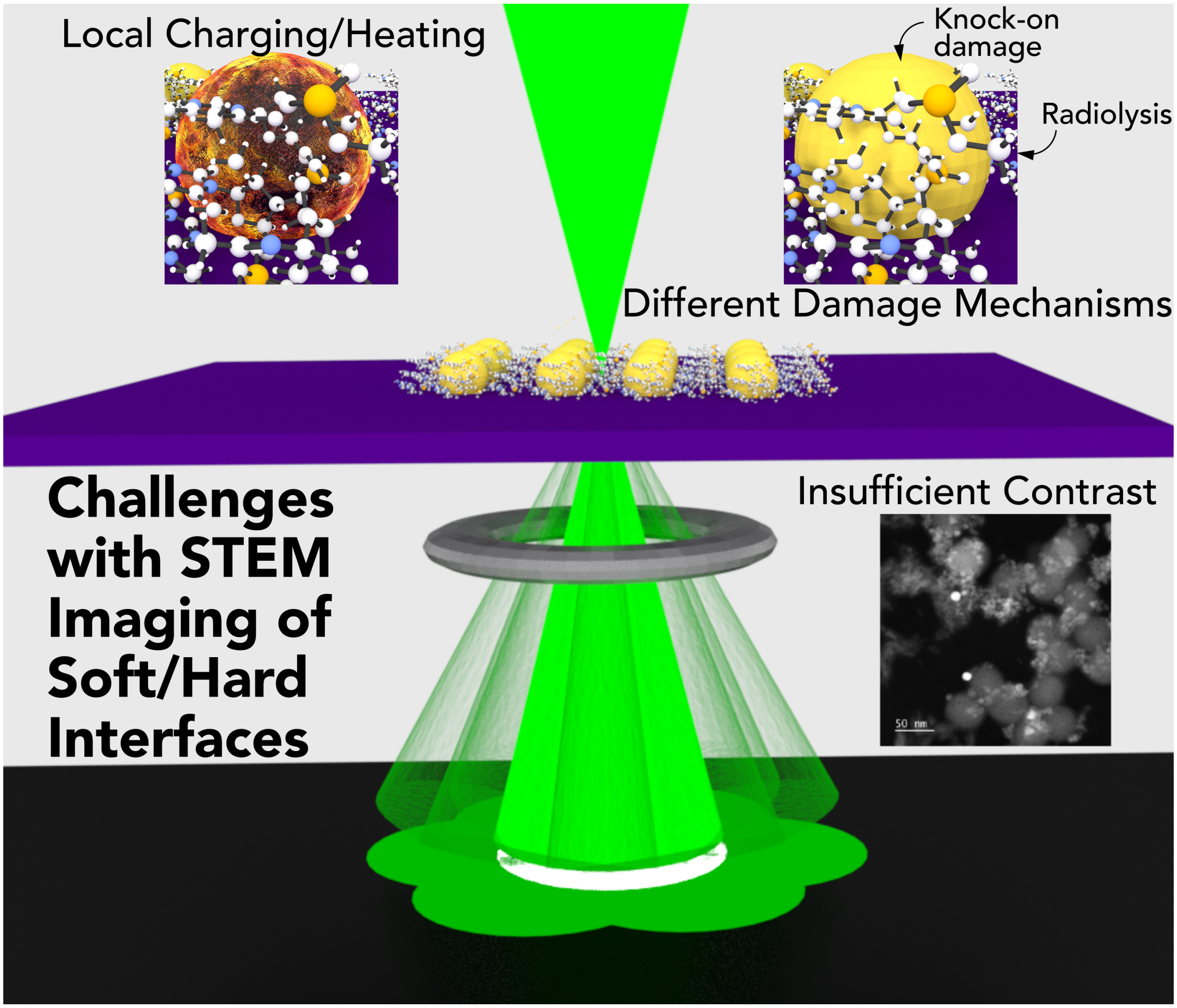

Figure 1: Challenges associated with imaging Hard/Soft Interfaces with STEM. These include local charging/heating, a discrepancy in beam damage mechanisms and inadequate image contrast between the different material components.

1.2 Challenges Associated with STEM Analysis of HSI

While the behavior and performance of materials can result from structures encompassing a wide variety of length-scales, in many cases, the critical or deterministic features tend to be on the nano or molecular-scale. Both conventional transmission electron microscopy (CTEM) and scanning transmission electron microscopy (STEM) are indispensable tools for understanding HSI in these materials. The spatial resolution of the spectroscopic and analytical techniques concomitant with STEM, such as energy dispersive X-ray spectroscopy (EDS) and electron energy loss spectroscopy (EELS), make it possible to identify local chemical, vibrational, electronic, and/or magnetic fluctuations of materials.[33–36] Here, we focus solely on STEM as the multimodal nature of its analytical and imaging techniques offer practical tools for probing these interfaces at the nano or molecular scale .[37–40]

STEM requires thin, electron transparent samples, so careful sample preparation is essential to preserve the sample integrity and avoid spurious signals.[41] Even when their natural structure is preserved, specimen damage resulting from electron radiation can take on many forms including knock-on damage (the displacement of atoms from the crystal lattice), radiolysis (inelastic ionization), charging, and/or heating.[42,43] In general, soft materials tend to be more prone to electron beam damage than hard materials. For instance, in the case of a hybrid inorganic/organic perovskite material, replacement of the inorganic Cs^+ ions with organic $CH_3NH_3{}^+$ ions leads to a structure that can withstand multiple order of magnitude decrease in the dose rate (100 $e^-Å^{-2}s^{-1}$ to 4 $e^-Å^{-2}s^{-1}$) and cumulative dose ($\sim$1000 $e^-Å^{-2}$ to $\sim$1 $e^-Å^{-2}$) at room temperature.[44–46] Metal organic frameworks, or MOFs, another hybrid structure, can withstand a room temperature dose on the order of 10-20 $e^-Å^{-2}$.[47] As such, the softer material limits the overall dose when imaging HSI and makes it difficult to obtain adequate signal from both constituents present as highlighted in Figure 1.[48]

The accelerating voltage also plays a role on the damage threshold as soft materials are particularly prone to radiolysis,[49] which scales with decreasing electron beam energy, while hard materials are particularly prone to knock-on damage,[50] which scales with increasing electron beam energy. This makes it challenging to entirely avoid beam damage in the critical interphase and interfacial regions. Nonetheless because the obtainable spatial resolution depends on the dose rate the specimen can withstand before degradation of the measured signal,[43] mitigating these sources of specimen damage while simultaneously boosting signal is essential in order to acquire high resolution images of hybrid interfaces.

Some of the most commonly employed tactics to mitigate beam-induced damage and/or boost signal include staining[51–53] and cryo-EM.[54] Unfortunately, neither of these proven methodologies adequately addresses the additional complexity introduced when a hard component is present. In the case of staining, the heavy metal scattering agent obscures the internal structure of the object, often compromising resolution.[55] On the other hand, cryo-EM has been a revolutionary advance that minimizes secondary effects from the initial electron-sample interaction and leads to an overall decrease in beam damage in soft materials.[56,57] However, this method alone does not address the discrepancy in contrast between hard phases and soft phases.

1.3 Review Outline and Scope

In this review, we discuss the role that STEM can play in interrogating HSI by summarizing recently developed techniques and proposing new solutions for addressing challenges associated with imaging HSI. It is intended for material scientists, chemists, and physicists interested in applying STEM techniques to unravel the complex chemical and physical structure of hybrid materials. We first discuss the inherent complexities associated with preparing thin, hybrid composite specimens and a few specialized methods that perform well despite aforementioned constraints. We then discuss how recent experimental advances throughout the entire experimental workflow beginning with sample preparation, followed by imaging and post-processing methodologies, provide a route to attaining improved contrast and image quality from hard/soft interfaces (Figure 2). We then detail the use of STEM tomography to attain rich three-dimensional information and the use of *in situ* approaches to explore the dynamical evolution of such interfaces. Finally, we discuss ongoing advances and best practices related to microscopy data management that will unlock more opportunities to attain holistic sample information in the future.

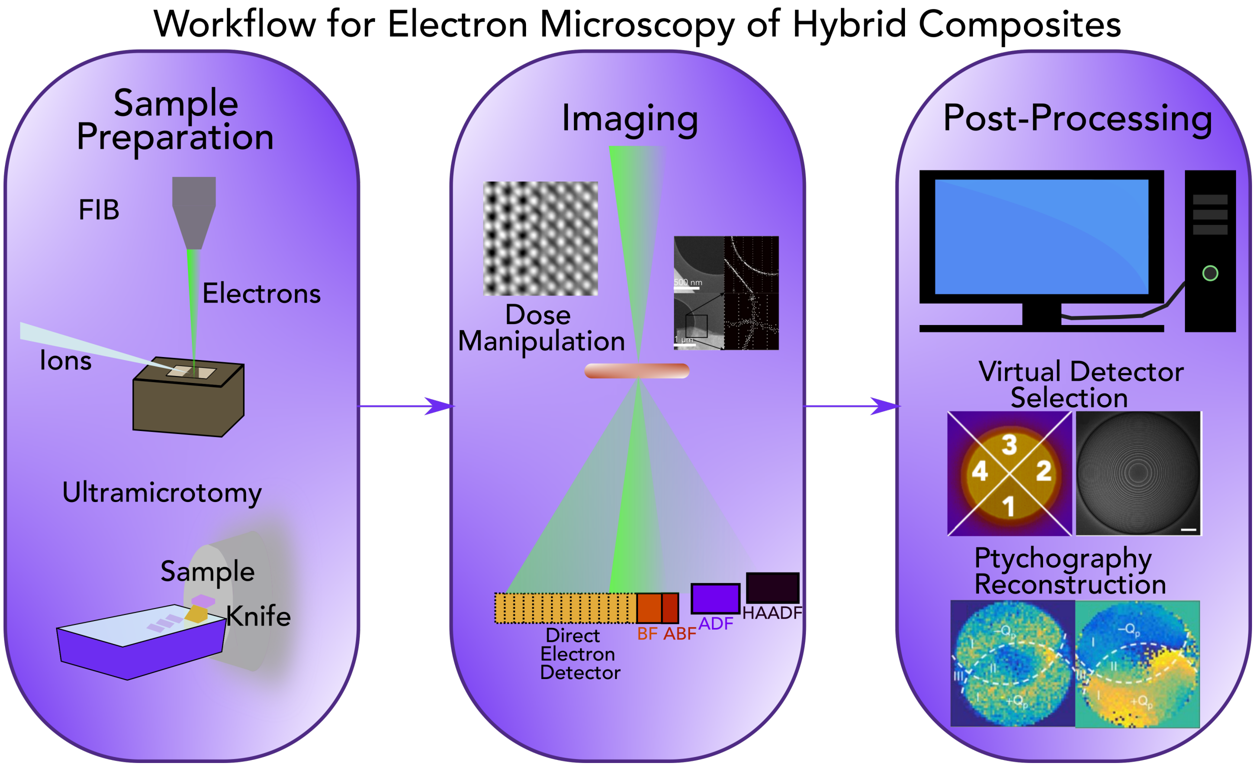

Figure 2: Recent advances throughout the entire electron microscopy workflow. For sample preparation, these include advances in focused ion beam and ultramicrotomy techniques (Section 2). With regards to imaging, manipulating the electron dose and direct electron detectors present two opportunities for preserving structural detail in HSI. Finally, post-processing techniques such as the use of virtual detectors or ptychography reconstructions present solutions for addressing these prevailing challenges (Section 3). Images from.[58–61]

2 Specialized Sample Preparation

Sufficiently thin samples that accurately represent their bulk counterparts must be carefully prepared in order to fully access the variety of signals and information available through STEM. Although simple drop-casting methods can be used for hybrid composite systems such as nanoparticle-DNA hybrids,[62,63] preparation of HSI samples can generally be quite challenging. The mismatch in mechanical properties present at HSI creates the need for refined sample preparation methods in order to adequately preserve these interfaces for subsequent microanalysis. Here we provide a breakdown of two specific techniques that have recently received much attention for site-specific isolation of HSI: ultramicrotomy and focused ion beam milling.

2.1 Ultramicrotomy: Generating cross-sections of diverse samples

Ultramicrotomy is traditionally used for the analysis of cells and biological tissue embedded in an epoxy resin,[64,65] however, many hard,[66,67] soft,[68] and hybrid materials[22,69] can also be prepared with this method.[70] This technique uses an ultramicrotome in conjunction with a glass or diamond knife to produce ultrathin (40-200nm) cross-sections of material. Biological samples are chemically processed through a series of aldehydes and osmium tetroxide, before being dehydrated and embedded in an epoxy resin. The solidification of this matrix produces a rigid sample for sectioning. A similar technique of embedment with epoxy resin can be used with hybrid systems such as MOFs or nanoparticle-DNA conjugates. Alternatively, bulky materials exhibiting glass transition temperatures (T_g) above room temperature can be mounted onto the ultramicrotome and directly sectioned.

In situations where the soft constituent displays T_g below room temperature, ultramicrotomy can be employed at cryogenic temperatures or with an ultrasonic diamond knife. While the former variant can initiate compression artifacts, the use of an ultrasonic diamond knife, which utilizes a piezo-electric crystal to oscillate the diamond blade in the x-direction relative to the orientation of the block face, can be operated at room temperature and typically leads to minimal compression artifacts.[71] Large differences in hardness between hard and soft components can further lead to artifacts such as tears, where the harder material is pulled out of the matrix, displacement of softer materials in the membrane or chatter, in which lines form in the specimen parallel to the knife edge.[72] Generally, these artifacts can be mitigated by carefully varying the cutting speed, the cutting angle, or the orientation of the knife blade.[72]

2.2 Focused Ion Beam (FIB): Site-specific thinning

FIB milling is another versatile method for preparing a broad variety of hybrid composite samples. This includes carbon fibers in epoxy matrix, where the use of FIB makes it possible to preserve the important interphase region that dictates the mechanical performance of such composites.[73–76] For biological hybrid composites, FIB has been exploited to prepare lamella of teeth, bones, and nacre.[5,77,78] In this case, the use of FIB enables subsequent high-resolution imaging of chemical gradients. For electronic architectures, FIB has been employed to isolate HSI present in photovoltaics[79] and flexible electronics.[80] Moreover, the ability to micromachine samples on the nanometer length scale has made FIB attractive for fabricating and positioning samples on specialized grids for 3D tomography as well as *in situ* analysis (Sections 4.1 and 4.2).[81,82]

This method involves milling and isolating a region of interest with a nanometer-scale ion probe. The lamella is then cut free and welded onto a TEM grid where it is thinned with the ion beam such that it is electron transparent for STEM analysis.[83–85] As the grazing incidence angle of the ion beam used for sample thinning leads to milling rates that are largely material independent, FIB is especially useful for preparing specimen from heterogeneous hybrid samples.[83] Additionally, this methodology provides site-specific highly uniform, thin sections, which are quite ideal for ensuing STEM imaging and EELS analysis.[85] Finally, through advances in cryogenic sample preparation, the soft constituents can be sectioned in their vitrified state, which is useful for minimizing the amount of beam damage present at a HSI.[86–88]

The milling process, however, can introduce various sample artifacts. For instance, charged ions can cause surface amorphization or become preferentially implanted and form defects in the soft and/or hard components of the sample. This effect can, however, largely be reduced if a low energy (50eV-1keV) and low current milling process with gallium or argon ions is performed immediately afterwards.[89–91] Another concern is redeposition of atoms on the sample surface following removal by the ion beam. This can be largely reduced by carefully maintaining a beam current compatible with both hard and soft constituents at each step of the process as well as using a local barrier to preserve the area of interest.[92,93] Finally, FIB milling can be quite time consuming, which limits its utility in isolating macro interphase regions within hybrid samples.

3 Advanced STEM Methods for Analysis of Soft/Hard structures

Recent STEM developments present new opportunities for probing and analyzing hybrid structures and HSI. In the following sections, we will first discuss the advantages provided by direct electron detectors (DEDs), a major hardware advance. We will then discuss a variety of analytical methods enabled by this technology to enhance interfacial contrast while maintaining structural integrity.

3.1 Direct Detectors: Reduced threshold dose and improved contrast

The introduction of DEDs has revolutionized the understanding of nanoscale features in biological and soft material systems over the past decade.[57,94,95] DEDs have brought to bear massive improvements in both detection efficiency and noise floors by eliminating the need for electron-photon conversion via a traditional scintillator and fiber optical plate setup, substantially increasing the detective quantum efficiency.[96–98] It is now possible to image beam-sensitive sample with reduced electron beam fluxes, which has had profound implications for attaining atomic resolution information of highly sensitive samples, such as COFs and MOFs.[99–101]

The high speed, microsecond range readout of DEDs makes it a practical tool to record multidimensional datasets, such as a convergent beam electron diffraction (CBED) pattern or spectral data at each probe position.[102–104] The ability to record a 2D diffraction pattern at each 2D probe position produces a four-dimensional dataset, which is referred to as 4D-STEM. Because CBED patterns contain rich chemical and physical phase information about a sample, this technique unlocks vast structural information about a specimen in addition to allowing for the reconstructiion of traditional imaging modalities. 4D STEM has grown in concert with the use of DED and will be further discussed in Section 3.2.[105]

3.2 Advances in STEM Acquisition and Reconstruction Methods: Simulated & experimental data

In traditional STEM, physical detectors are used to selectively capture forward scattered electrons falling within a pre-defined angular range. Transmitted electrons displaced within the angular range defined by the electron probe convergence angle are captured by a circular detector to generate bright field (BF)-STEM images . Annular dark field (ADF)-STEM refers to a class of techniques where images are generated using an annular detector to capture transmitted electrons scattered outside this bright field range, including high angle annular dark field (HAADF)-STEM. Electrons from the primary beam are scattered to large angles as a result of incoherent and elastic interactions with the sample.

In BF-STEM mode, electron signal is the result of complex interplay between thickness, diffraction, and compositional effects. Conversely, in ADF-STEM mode, electron signal is dominated by elastic Rutherford scattering and is more easily interpretable.[106] Since the Coulomb interaction between atomic cores and incident electrons increases as the effective nuclear charge increases, ADF signal intensity is related to the atomic number (Z) of the constituent atoms in the sample. As a rule of thumb, ADF signal intensity is proportional to Z^{α}, where α lies between 1.2 and 1.8 depending on the microscope conditions, collection angle, and sample.[107,108]

The challenges associated with applying these techniques to HSI can be most accurately described in terms of contrast transfer functions. When an electron beam interacts with the sample it produces an image composed of amplitude and phase components. In the case of non-linear imaging techniques such as BF-STEM, the relationship between the recorded image and the object functions is non-trivial due to the various contrast mechanisms previously discussed. In the case of approximately linear imaging techniques such as ADF-STEM, a linear convolution of the object function with the point spread function yields the recorded image intensity.[109–111]

Unfortunately, because ADF-STEM provides a linear image of the square of the phase of the object transmission function, it is far less sensitive to low Z elements and leads to significant variation in ADF signal intensity for materials with disparate chemical compositions. As a result, this substantial image contrast limits the ability to see fine features within adjacent materials at this heterojunction. To this end, there is a need for alternative imaging methods that are linear with the object transmission function. In the following sections, we discuss recent developments associated with a few of the most promising phase contrast imaging modalities that make it possible to simultaneously image heavy and light atoms.

As mentioned above, with a 4D-STEM dataset, BF and ADF images can be similarly generated by employing a user-defined ”virtual” detector during post-imaging analysis. This virtual detector, or binary mask, is applied to each diffraction pattern in order to preferentially select reciprocal space data falling within a specified collection angle range. Instead of collecting a single intensity value at every pixel position with a traditional monolithic BF/ADF detector, the 4D-STEM approach enables retention of the relationship between probe position and scattering angle distribution. Thus with a 4D dataset, the microscopist has the ability to construct BF and DF images of various collection angles by varying the virtual detectors following the experimental session.

To highlight this point and demonstrate conventional imaging modalities , we present a model hybrid composite system in Figure 3 composed of nanoparticles (hard) integrated within an epoxy matrix (soft) from which a 4D-STEM dataset was collected. By constructing a circular mask to capture electron signal deflected within the bright field disk (0 to 3.5 mrad), we were able to create the BF-STEM images seen in Figure 3A. Similarly, by creating an annular mask to capture electron signal deflected outside the bright field disk (3.5 to 25 mrad), the ADF image presented in Figure 3B was produced. As ADF-STEM offers limited sensitivity to low Z elements, the large discrepancy in signal between the nanoparticles and the neighboring matrix in Figure 3B makes it challenging to ascertain the fine features present at this interfacial region.

This approach can be taken a step further by tailoring collection radii to the scattering of various elements in a sample to create a map of different phases within a sample. Figure 3E shows the results of this strategy employed on the same dataset from A-C overlaid on a bright field image. In this case, the ability to differentiate between elements is somewhat limited because there is overlap in the distribution of their scattering angles in reciprocal space and because the dataset is noisy, a constraint imposed by the soft epoxy matrix. Nonetheless, the relative consistency between the EDS map (Figure 3F) and the chemical classification map based on forward scattering suggests that these methods can complement each other in identifying compositional heterogeneities in a wide variety of system. Additionally, forward scattering-based classifications offer advantages over EDS methods in that they can demonstrate a high collection efficiency, which leads to much faster data collection.

There is substantially more information than shown in Figure 3 that can be obtained with 4D data. Because CBED patterns are quite sensitive, subtle changes in the pattern location and intensity on the detector can be related to the local lattice spacing.[112–114] This sensitivity makes it possible to identify variations in local structure and strain fields at HSI. We will discuss some of these techniques in later sections, and Ophus provides a comprehensive review of 4D STEM techniques.[103]

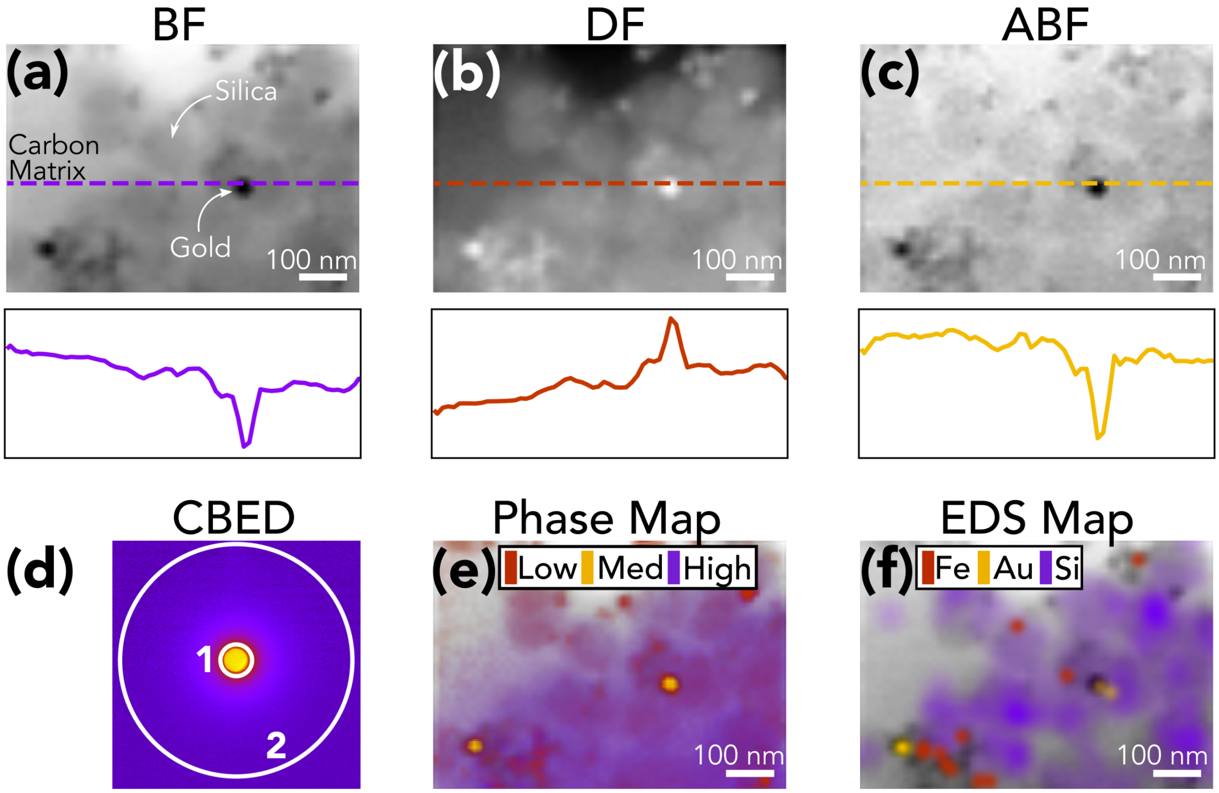

Figure 3: Imaging of model hybrid composite system composed of Au, Fe_3O_4, and SiO_2 nanoparticles embedded in a carbon matrix with a probe convergence semi-angle of 3.5mrad to achieve a Kossell-Möllendsted pattern, which provides good separation of disks for easier phase mapping. (A) BF (<3.5 mrad, detector is area within in ring 1 as shown in (D)). (B) DF (3.5-25 mrad, detector is area outside the central disk and between ring 1 and 2 as shown in (D)). (C) ABF (2.3-3.5 mrad), detector is outer third of area within ring 1 (D)). Normalized line profiles in A-C show change in contrast and signal to noise. (D) CBED averaged across entire sample area. (E) Phase map superimposed on BF image. Color indicates sensitivity to phase defined by low (3.5-5.3 mrad), medium (5.8-7 mrad), and high (8.8-26 mrad) collection angle ranges using virtual detectors. Counts in arbitrary units. (F) EDS map superimposed on BF image. Color indicates normalized x-ray counts. EDS has a small collection angle, making it a dose inefficient method and leading to a sparser dataset that misses some of the nanoparticles. However, with a phase map it is more difficult to distinguish materials with a similar Z or amorphous components, such as in the case of SiO_2 and C, which is not a limitation of EDS.

3.2.1 Annular Bright Field (ABF) Imaging: A route to visualizing heavy and light atoms

In annular bright field (ABF)-STEM, an annular detector collects electrons scattered to the outer edge of the bright field disk.[115,116] This method is compatible either with physical or virtual annular detectors. Due to the relationship between electron channeling effects and electron intensity in this region of the bright field disk, this method allows for simultaneously observing both heavy and light elements as described through three generalized situations detailed by Findlay et al..[117] For instance, in a situation where an electron probe is placed between adjacent atomic columns, a uniformly intense bright field disk with minimal dark field intensity would be generated. If, instead, this probe were aligned with a column of light elements, a greater proportion of electrons would be scattered to the dark field and the center-most bright field regions due to electron channeling effects, which leads to a reduction in electron intensity to the outer area of the bright field region. Similarly, if the probe were aligned with a column of heavy elements, a greater degree of electron scattering into the dark field region yields an overall decrease throughout the entire bright field region.[117] While a more comprehensive description of image formation mechanisms that serve as the foundation for ABF signal in hard and soft materials is provided by Okunishi et al. and Findlay et al.,[118,119] the intensity variations in the outer area of the bright field region associated with this conceptual model suggests that unlike ADF, this method yields appreciable electron signal from both hard and soft materials.[120]

From Figure 3C, we find that this imaging modality does indeed boost signal and structural detail from the soft components in the sample (the epoxy matrix). An optimized collection angular range consisting of the outer third of the central disk produces substantial imaging contrast of these components within the sample.[117,118,121] This enhanced contrast has made ABF quite popular for imaging lithium ions and there exist several recent reports and review articles dedicated to this topic.[122–126] ABF has similarly made it possible to image carbon shells on metallic nanoparticles[127] and the presence of hydrogen atoms in a YH_2

crystal.[128]

ABF presents limitations, however, when addressing HSI. For instance, because ABF signal intensity mainly arises due to coherently scattered electrons , variations in crystal orientation or strain make it challenging to quantitatively assess the chemical nature of various constituents.[129] Furthermore, as Findlay et al. show, the non-linear nature of this imaging modality leads to contrast reversals across specific thickness, tilt and defocus ranges.[119,129] Also, because the only electrons retained for image reconstruction are those that fall within a narrow band of polar scattering angles within the bright field disk, the signal-to-noise ratio (SNR) of this method lags other phase contrast imaging techniques and information associated with higher spatial frequencies is lost as well. One method to mitigate these issues would be to combine this signal with signal from incoherently scattered electrons as in the incoherent bright field (IBF)-STEM method. This method allows for imaging hybrid samples with thicknesses exceeding 100 nm.[130,131] Nonetheless, the collection of both coherent and incoherent electrons can produce data interpretation challenges, which are mitigated with emerging phase contrast techniques discussed in the following sections.

3.2.2 Differential Phase Contrast/First Moment STEM: A means to detecting subtle phase shifts

Because the phase component of the sample transmission function can impart a physical shift on the beam illumination at the detector plane, another phase contrast approach would be to examine methods that characterize this subtle spatial variation. To this end, the similar methods proposed by Dekkers and de Lang (differential phase contrast - DPC) in 1974 and Waddell and Chapman (first moment STEM - FM-STEM) soon thereafter have recently received interest, as the introduction of DEDs have made these methods practically employable.[132,133] The former method involves measuring the difference in electron signal captured within opposite regions on a divided detector, such as quadrant detector, at each probe position to calculate deflections in the transmitted beam in x and y directions as a function of spatial location in the sample plane. The latter method involves measuring the intensity center of mass (I_{COM}) of the beam illumination at the detector plane. In recent years, it has been proven that the momentum transfer that the electron probe experiences and calculated through FM-STEM is linearly related to the gradient of the phase of the specimen transmission function. Meanwhile, the signal captured by DPC serves as a less computationally expensive, useful approximation for this gradient.

DPC images of hard and soft nanostructures embedded in an epoxy matrix are presented in Figure 4. Compared to ADF, it is apparent that recovering the phase component without sacrificing signal in the bright field disk through DPC reduces image contrast between both hard and soft components. These images were constructed by filtering the 4D dataset with the virtual quadrant detectors seen in Figure 4D. Recently, Lazić et al. proposed a variant to these methods by showing that the integrated COM and DPC signals across the 2D bright field detector (iCOM and iDPC) are linearly related to the phase of the transmission function of the sample.[134] In the context of HSI, this purely phase image has made it possible to identify low Z elements, such as O and even H.[135–138] The divergence of the COM and DPC signals, dCOM and dDPC, are proportional to the projected charge density within the sample and are particularly useful in the context of atomic resolution imaging and modeling electrostatic interactions at interfacial regions. iDPC and dDPC images of the nanoparticle-matrix sample are provided in Figure 4E-F. As these methods produce appreciable signal from both hard and soft materials, a distinct improvement in relative contrast is evident in both images. The enhanced signal in both iDPC and dDPC at the edges of the nanostructures likely results from the accumulation of charge at the matrix/nanostructure interface that may result from carbon buildup during imaging as discussed previously by Lazić et al.[134]

These methods have emerged as a popular tool for imaging hybrid structures such as zeolites,[139–141] and complex oxides.[142–144] Further, the dose-efficient nature of this method allows for obtaining adequate signal from sensitive materials within the sample's dose limit.[145] Although DPC and COM-based techniques offer significant advantages over ABF including a

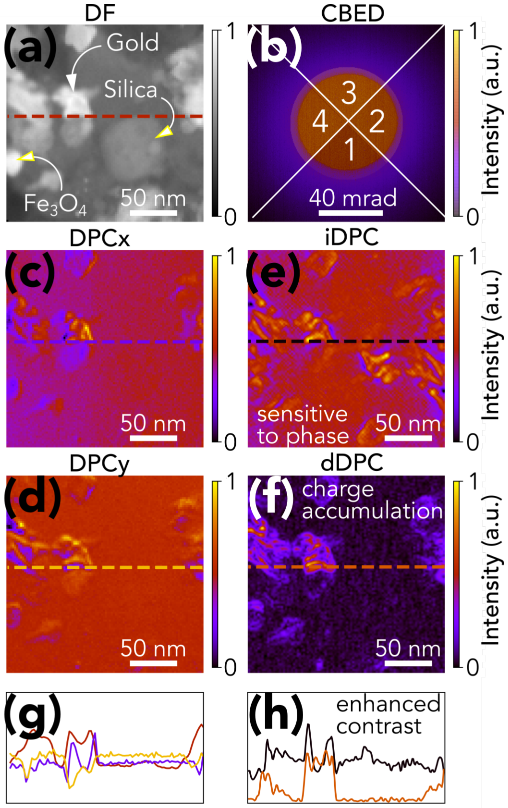

Figure 4: DPC imaging of sample of Au, Fe_3O_4, and SiO_2 nanoparticles embedded in a carbon matrix with a probe convergence semi-angle of 30 mrad to obtain to achieve optimal spatial resolution. The dotted lines in the image represent regions over which intensity line profiles were acquired. (A) DF (3.5-25 mrad). (B) Quadrant detector employed to produce differential signal. Electrons captured in opposite detectors were subtracted from one another. (C) DPC_x (Detector 2 - Detector 4). (D) DPC_y (Detector 3 - Detector 1). The DPC images provide much greater contrast between the soft, lightly scattering components and the background. (E) iDPC image produced by integrating the DPC signal across the bright field disk. iDPC provides an accurate representation of the phase component imparted by the sample (F) dDPC image produced by taking the divergence of the DPC signals. dDPC is proportional to the projected charge density within the sample. iDPC and dDPC both provide improved interfacial detail. (G) Normalized line profiles show change in contrast and signal to noise between the ADF, DPC_x, and DPC_y images. (H) Normalized line profiles show change in contrast and signal to noise between iDPC and dDPC images. The enhanced signal in both iDPC and dDPC at the edge of the nanostructures may result from the accumulation of charge or carbon buildup at the matrix/nanostructure interface.

contrast transfer function that is far easier to interpret, sources of diffraction contrast can also contribute to probe deflection and introduce imaging artifacts.[146] Additionally, although iDPC is a highly implementable approximation of iCOM signal, increases in thickness can cause this approximation to break down and generate contrast reversal effects in areas where the defocused probe interacts with the sample. This increase in plural and inelastic scattering with increasing sample thickness is responsible for this break down in the approximately linear relationship between iDPC contrast and the sample's transmission function.[138,147] Additionally, iDPC and iCOM largely remain empirical techniques and a comprehensive understanding of contrast mechanisms in different systems requires continued exploration.

3.2.3 Ptychography: A dose efficient method for phase retrieval

The original motive of using electron ptychography in STEM was in the context of improving spatial resolution beyond the resolution limit set by the microscope lenses.[105,148] Nowadays, however, the most important outcome of this computational imaging method is that it produces a complex image encompassing both amplitude and phase of the exit electron wave after interaction with the sample.[149]

In practical terms, ptychography retrieval methods are conducted by taking the Fourier transform of the CBED pattern captured at each position in real space. In the case where the resultant diffracted beams in the 4D dataset overlap one another, the interference pattern formed in the overlapping region contains both phase and amplitude information that can be distinguished from one another by integrating selected areas of this matrix.[149,150] There exist several algorithms for recovering the phase information with each offering various advantages depending on the materials complexity and electron dose. These include the extended ptychographic iterative engine (ePIE), an iterative Fourier ptychography method that starts from initial guesses for the probe and object functions followed by a series of forward scattering calculations to determine the probe and the exit-wave.[105,151,152] Additionally, non-iterative algorithms involving only Fourier transforms and deconvolutions, such as Wigner-distribution deconvolution (WDD) method[153] and the single sideband (SSB) method,[150] which assumes a weak phase object, have been developed. One advantage of WDD and SSB methods is the possibility of including residual aberrations to further tune the reconstruction quality.[60,149]

Additionally, the application of extremely low electron doses (e.g. $< 1\mathrm{e}^-/\text{Å}^2$) still results in scattering events that are distributed across many pixels in the detector. Ptychography can be efficiently applied to retrieve these events and consequently reconstruct the object function by making use of the entire bright field region.[150,153–155] Defocusing the probe can also lower the total amount of electron dose applied to cover the region of interest by reducing the number of probe positions necessary.[154] Moreover, recent developments associated with focused probe ptychography make it possible to complement ptychography reconstructions with high resolution ADF images as well as EDS and potentially EELS maps to attain compositional information in addition to structural details of hybrid structures.[60,156]

Thanks to advances with DEDs, electron ptychography has been employed on a wide variety of materials systems. Since applied to study silicon by Nellist et al., it has since been used for materials such as graphene,[157] GaN,[158] Ti and Nd-doped $\mathrm{BiFeO_3}$,[158] halide perovskites,[159] and complex carbon nanotube conjugates.[60] These studies highlight the advantages of ptychography for hybrid materials, as both heavy and light, beam-sensitive elements can be imaged simultaneously. Researchers are pushing the boundaries of how to more efficiently reconstruct information using lower doses for beam sensitive materials, such as with binary imaging or compressive sensing, which makes it very useful for obtaining sufficient signal while minimizing the aforementioned damage mechanisms present at HSI.[154,160,161] The ePIE method is very effective when using defocused probe datasets which allows further electron dose reduction and was recently used to reconstruct data obtained from biological samples at doses as low as $5.7\ \mathrm{e}^-/\text{Å}^2$.[162]

Here, to demonstrate the applicability and the benefits of ptychographic reconstruction in systems containing HSI, we utilize a model system of a gold/carbon interface. The 4D dataset was simulated as described in S1.4 without probe aberrations, and the ptychography reconstruction performed using the SSB method.[157] In our example, we highlight two major characteristics that can be leveraged using electron ptychography: electron dose efficiency and resolution improvement. Figure 5 shows how SSB ptychographic reconstructions of standard and low electron dose images can enhance structural details of both hard and soft components compared to ADF images. This is due to high efficiency information transfer across a broad spectrum of spatial frequencies in the case of ptychography compared to ADF.

Nonetheless, there are some significant drawbacks for this method. For instance, ptychography reconstructions require caution when dealing with samples that violate the weak phase object condition and are likely to exhibit dynamical scattering effects. To overcome this issue, novel methods based on multislice ptychography as well as closely related techniques such as optimum bright field have been developed.[163,164] Moreover, generating reconstructions of the large 4D datasets commonly collected for ptychography can require significant computational power and storage space. This necessitates massive improvements in the STEM data workflow which we will discuss in Section 4.3.

3.2.4 Modifying Incident Electrons: phase plates

Phase plates, mostly in the form of the Zernike and the Volta geometries, are well known tools in cryo-TEM to enhance phase contrast in images without the need for a significantly defocused beam.[165–167] These plates impose a phase shift on the electron wave and as such, the resultant interference between transmitted and diffracted electron beams produces an intensity variation that can be linked to the phase component introduced by the sample. Recent reviews have proposed opportunities for expanding the use of phase plates, but to date, have predominately been limited to conventional cryo-TEM.[168–171] There has been growing interest in using a similar approach in STEM to collect phase information by manipulating the shape of the electron beam, including creating vortexes, concentric Fresnel rings, and bullseye patterns.[112,114,172–174]

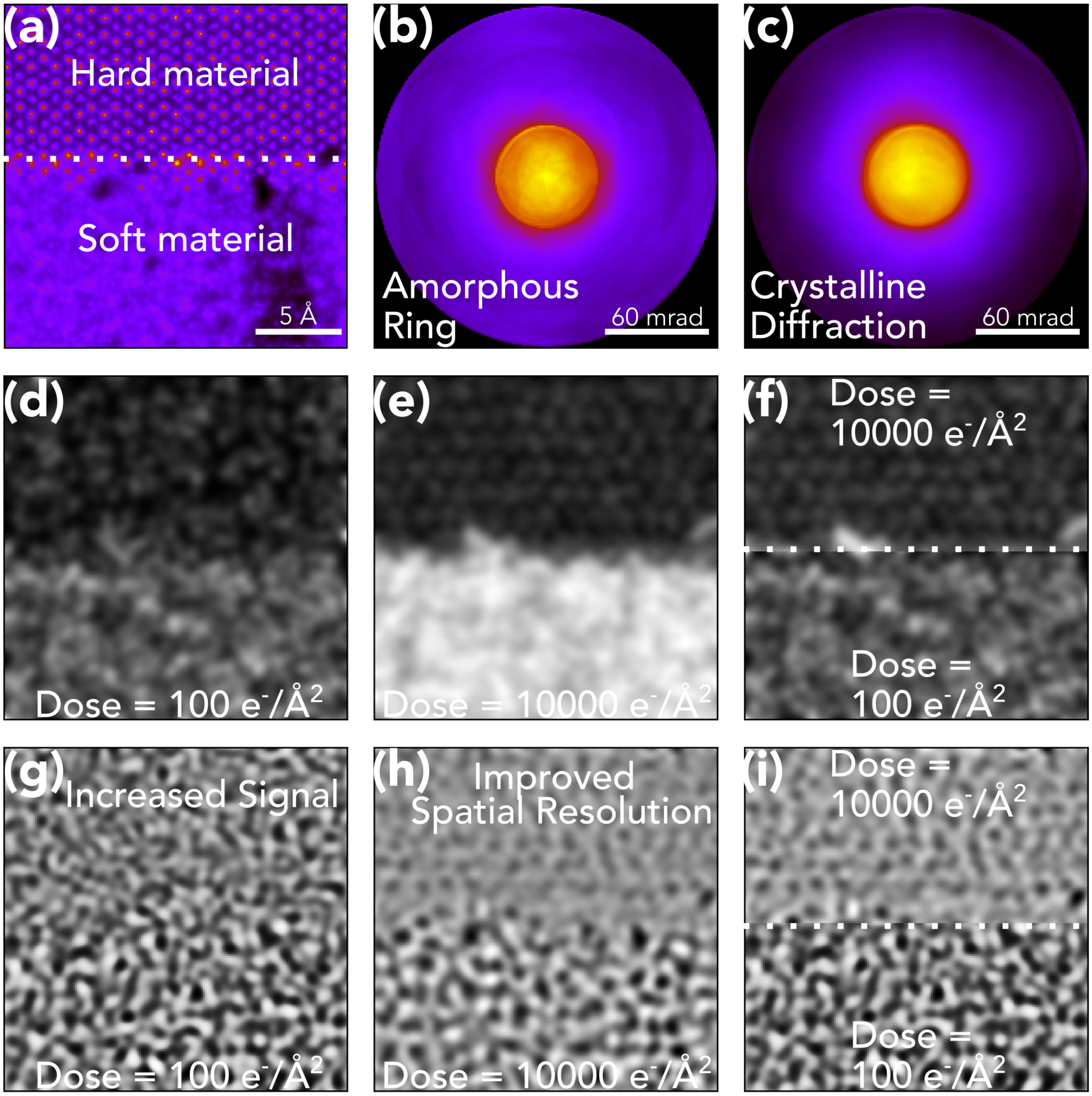

Figure 5: STEM simulations of gold/carbon matrix interface (A) The projected potential of the sample. (B-C) The corresponding simulated diffraction patterns taken from the hard (B) and soft regions with a probe convergence semi-angle of 30 mrad to increase the level of overlap between diffracted disks and increase spatial resolution (C), respectively. (D-E) Simulated ADF images taken with a relatively low dose (100 $e^-/Å^2$) (D), and a higher dose (10,000 $e^-/Å^2$) (E). (F) Adaptive sampling method where the low dose is applied to the soft component and the higher dose is applied to the hard component to preserve its structure during ADF imaging. (G-H) Simulated ptychography reconstructions at these low (G) and high (H) dose values produce improved interfacial contrast and spatial resolution from the hard material region. (I) Similar adaptive sampling method applied in (F) followed by ptychography reconstruction.

The rising popularity and availability of the direct detector in combination with the phase plate has led to further developments in imaging HSI. A near linear phase imaging technique called Matched Illumination Detector Interferometry (MIDI-STEM) incorporates a virtual detector whose geometry matches that of the Fresnel phase plate.[61] The strength of the MIDI-STEM technique is in its ability to image heavy and light elements at HSI due to its alternating ring geometry that enhances the transfer of low spatial frequency information within the allowable dose limits set by the soft material. The phase component stored at high spatial frequencies of these images can be even further enhanced with the incorporation of both a pre-specimen phase plate and ptychography, as shown by PMIDI-STEM (Ptychography MIDI-STEM).[175] A similar approach was used by Tomita et al., who inserted an amplitude Fresnel zone plate into the probe forming aperture of a microscope in a STEM configuration to increase the contrast transfer function for low spatial frequencies when imaging light materials.[176] Overall these phase plate techniques are powerful and their dose efficient nature allows for discerning fine features in hard and soft materials simultaneously.

Here we use simulations to demonstrate some of the advantages of using a combined phase plate, direct detector approach. We focus on the step-edge junction that forms when $MoTe_2$ is stacked upon a graphene substrate such has been demonstrated for photodetector applications.[177]

For the purpose of this simulation, an electron beam was first convolved with a Fresnel phase plate at the probe forming aperture. This created a beam with rings of alternating phases of 0 and $\pi/2$. Following the interaction of the modified probe with the sample, the resultant 4D dataset was filtered through a virtual detector exactly matching the illumination pattern incident on the sample. Figure 6A shows the phase of the control probe as compared to the modified probe in Figure 6B. The CTF of the modified probe is shown in Figure 6C and shows strong information transfer at low spatial frequencies.

Compared to the projected potential (Figure 6D), the conventional dark field images (Figure 6E) show the expected challenges with attaining sufficient electron signal from both carbon and the heavier $MoTe_2$ atoms at the same time. However, the resulting image captured with a Fresnel plate in Figure 6F shows significantly improved relative contrast between the hard and soft components. This is emphasized by the line profiles in Figure 6G.

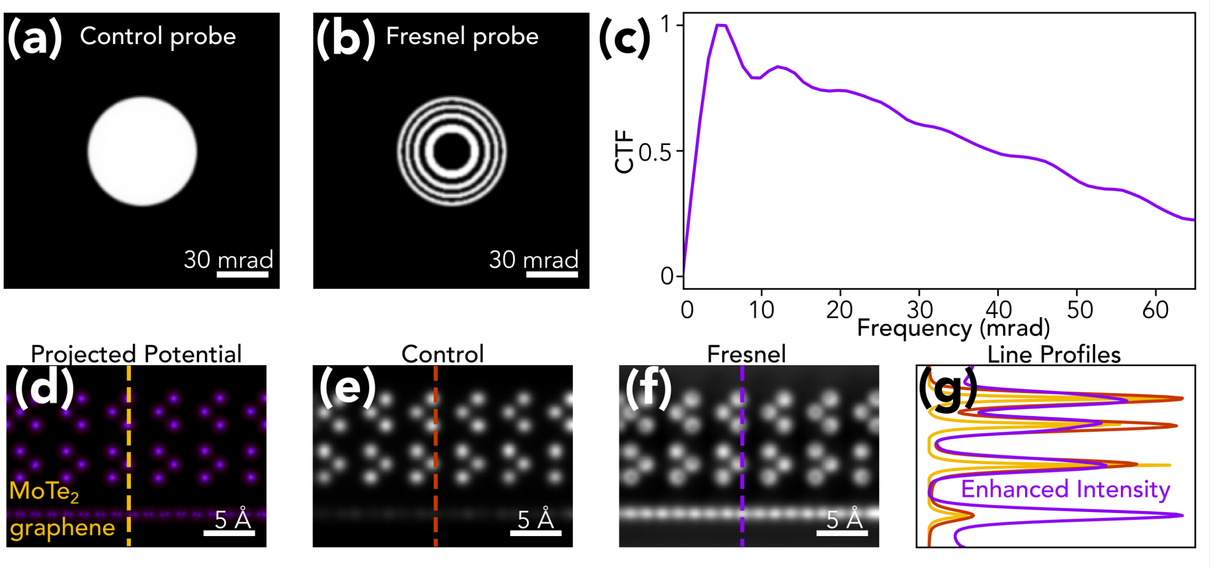

Figure 6: Phase plate study of a molybdenum ditelluride/graphene layered heterostructure. Phase of the (A) control and (B) Fresnel probe before sample interaction. (C) The contrast transfer function for the modified probe. (D) Projected potential of graphene/$MoTe_2$ sample. Conventional (E) dark field (35-120 mrad) image of the area. (F) Image of same region with Fresnel probe, showing improved contrast between heavy and light elements. (G) line profile comparing contrast from (D)-(F).

Although phase plates have the potential to be an incredibly useful imaging technique, there exist challenges associated with aligning these apertures in the microscope and characterizing the initial probe. Moreover, thin film phase plates are prone to carbon buildup over time, which changes the phase shift and decreases the signal to noise. New electron phase modification techniques relying on lasers[178] or magnetic fields[179] are being developed to overcome these challenges and we anticipate continued growth in this area.

Comparison of STEM Acquisition and Reconstruction Methods

Technique	**Advantages**	**Limitations**
BF	• Appreciable signal from soft materials	• Multiple contrast transfer mechanisms limits analysis
ADF	• Linear imaging technique makes it possible to quantitatively discern chemical structure	• Insensitive to low Z elements • Dose-inefficient method
ABF	• Appreciable signal from soft and hard materials	• Presence of diffraction contrast sources can make it difficult to quantitatively discern chemical structure • Dose-inefficient method
DPC	• Appreciable signal from soft and hard materials • Dose-efficient method • Approximately linear imaging technique • Linear approximations can break down with increasing sample thickness	• Diffraction contrast can generate imaging artifacts • Requires fast electron detector or quadrant detector

Technique	**Advantages**	**Limitations**
Ptychography	• Appreciable signal from soft and hard materials • Dose-efficient method • Allows for improving spatial resolution beyond the resolution limit set by microscope lenses • Approximately linear imaging technique	• Typically requires specimen thickness on the order of few atomic layers • Can be computationally expensive depending on reconstruction algorithms • Requires fast electron detector for high resolution
MIDI	• Approximately linear imaging technique yields improved signal from lower spatial frequencies common in amorphous materials • Appreciable signal from soft and hard materials • Dose-efficient method	• Practical challenges with phase plate preparation and alignment • Requires fast electron detector for high resolution

Table 1: Discussion of advantages and limitations associated with various STEM acquisition and reconstruction techniques.

3.3 Dynamic/Sparse imaging: Image reconstruction from undersampled datasets

3.3.1 Compressive Sensing: Image reconstruction through inpainting

As described previously, the soft material sets an upper limit on dose at a HSI, putting restrictions on overall signal to noise. One approach that is used for minimizing the electron dose and damage that soft materials experience is to deliberately sparsely image a sample and then employ a compressive sensing technique to reconstruct a complete image.[180] Sparse imaging offers a host of advantages for hybrid samples, including a reduction in the time over which the electron interacts with the sample. Although, hard and soft materials display differences in terms of damage mechanisms, a decrease in overall dose uniformly preserves the sample.

Compressive sensing is a broad technique rooted in many imaging fields but lends itself especially well to STEM (and SEM) because of its sequential acquisition mode. Here, we will focus on inpainting electron microscopy images to infill missing portions of the under sampled dataset.

While theory papers often rely on virtual image reduction, a physical beam blanker or externally controlled scanning coils are employed in practice. The relative importance of various factors such as acquisition time, location precision, beam stability and propensity for scanning distortions can dictate which method is used.[181–183] Researchers are continuing to test more exploratory methods for data acquisition, which inspire methods such as adaptive sampling that are particularly relevant for HSI as discussed in the next section. Likewise, there exist numerous approaches for reconstructing images from sparse datasets that run the gamut from image filtering to advanced machine learning algorithms.[183,184] The simplest approach is interpolation using data from nearest neighbors.[185] However, many algorithms have been developed that try to improve on this tactic by including learned information about the sample. One common method is a beta factor process analysis (BPFA) approach,[186] where a dictionary learning Bayesian model fills in missing pixels probabilistically from known elements for image restoration.[182,185,187–189] Additionally, there exist inpainting methods for suppressing the noise associated with undersampled data.[182] Recent work to develop more advanced approaches using convolutional neural networks, or deep learning algorithms assign weights to particular features in an image in order to assist in identification and reconstruction.[190]

In the context of heterogeneous hybrid samples, many of these compressive sensing techniques lend themselves especially well to this type of sample due to the ability to detect abrupt interfaces.[58,191] Moreover, compressive sensing can also be combined with the multimodal signals associated with STEM to interrogate interfaces with analytical STEM techniques, including EDS, EELS and cathodoluminescence.[58,189,192] This approach can also be used with 3D reconstructions, which will be discussed in more detail in Section 4.1. As with many advanced approaches, one limitation of this technique is the offline computation time needed to collect and analyze data. Despite the many benefits of inpainting, especially for materials with a beam sensitive component, this technique does not fundamentally improve contrast between hard and soft materials. One way to improve the SNR with this method is with a smart dwell time approach, which is discussed in the next section.

3.3.2 Adaptive dwell time: Intelligent sampling of the specimen

One of the main challenges in imaging HSI is that the soft material sets an upper limit for the dose that can be applied and the SNR that can be generated from the hard material. Scanning electron microscopy techniques have the advantage that they can decouple acquisition parameters with spatial position, making it possible to apply different doses to different areas of the sample depending on the local beam sensitivity. An example is shown in Figure 5F, and it is possible to imagine how such a scheme can be used in combination with ptychography (Figure 5I) or inpainting (discussed below).

This concept of adaptive dwell time has received recent interest in the microscopy community.[193] For example Timischl used a dynamic dwell time in a SEM based on signal statistics, which ultimately decreases dwell time for brighter pixels.[194] Another SEM method uses a two pass system, where the initial sample area is evaluated and then areas with high spatial frequency information are scanned again for more detailed analysis.[195] In an atomic resolution STEM setup, Stevens et al. used a similar adaptive sampling strategy where they applied an increased dose to regional maxima in a ZnSe sample and generated atomic resolution with doses on the order of 10 $e^-/\text{Å}^2$.[183] An adaptive dwell time approach has also been demonstrated for EELS and EDS data collection with a multi-objective autonomous dynamic sampling (MOADS) method. This on-the-fly dynamic approach reduces sample acquisition time and beam radiation while producing detailed elemental maps.[58]

These dynamic sampling techniques are far from routine practice, yet it is clear how they will be beneficial for hybrid materials. With the combination of interface detection, intelligent sparse data collection, adaptive dwell time, and inpainting, hybrid materials can be carefully characterized.

4 Emerging Opportunities & Outlook

To this point, we have discussed how a variety of recent advances associated with sampling and detection of STEM signals have enabled high-resolution imaging of HSI. Although we have mainly focused on 2D projections, these concepts can be extended further through the use of electron tomography to interrogate complex 3D systems. They can also be applied in tandem with *in situ/operando* STEM methods to understand the behavior of these interfaces when stimulated. Although these methods have the potential to provide a much more complete understanding of an HSI than conventional techniques , these investigations often generate large multidimensional datasets and can rely on computationally expensive reconstructions. These practical considerations are critical for widespread implementation of these methods. We conclude this section by discussing recent advances and best practices related to data management. An overview of this section is presented in Figure 7.

4.1 3D Reconstruction of Hard/Soft Interfaces: Electron tomography

STEM images are a 2D projection of a 3D structure, which in addition to creating complications in imaging and diffraction analysis, fundamentally results in missing information, even in the case of an ultrathin sample.[106] There are many techniques to reconstruct 3D information about a specimen, such as the use of STEM tomography for understanding the structure and properties of intricate nanostructures.[196,197] This technique involves capturing 2D images at a wide range of tilt angles, which are used to reconstruct a 3D representation of a region of interest.

The captured electron signal for tomography must meet the projection requirement such that it is a monotonic function that scales with a physical property of the system, introducing key questions about contrast that have been discussed throughout this review .[198] BF-STEM signal meets this criteria in the case of an amorphous material as mass thickness serves as the main contrast mechanism.[199] When a crystalline component is introduced, however, the projection criteria is no longer fulfilled due to the presence of a diffraction contrast term within the BF signal.[200] In this case, ADF signal is the natural alternative since Z contrast meets the projection requirement.[201]

Moreover, various groups have recently demonstrated that ADF signal can be used as the basis for atomic electron tomography (AET), a class of techniques that provides three-dimensional structural information from crystalline and amorphous materials with atomic resolution.[202–206] By pairing new iterative algorithms with an aberration corrected STEM using a direct electron detection scheme, an unprecedented level of spatial identification is now achievable , such as the spatial identification of defects, including grain boundaries, dislocations, and point defects.[202–204,207]

ADF electron tomography reconstructions of hybrid composites suffer from the same contrast challenges detailed in Section 3.2, making it difficult to examine materials with both heavy and light elements. As such, tomographic reconstructions employing advanced phase contrast techniques are needed to thoroughly understand interfacial morphology. Recently, a phase contrast atomic resolution tomography technique using high resolution TEM has been demonstrated.[208] This approach provides the ability to identify the location of light atoms, such as lithium, carbon, and oxygen in three dimensions. This TEM technique suggests how STEM methods described earlier, such as ptychography or use of a phase plate, combined with 3D tomographic reconstructions, can provide rich atomic scale information about hybrid materials.[209]

Due to limitations in the number of angular projections that can be acquired and the maximum tilt angle (70 °) attainable, tomography produces undersampled data. Although algorithms such as weighted back projection (WBP) and simultaneous iterative reconstruction technique (SIRT) have made it possible to mitigate the missing wedge effect and reconstruct a wide variety of hard and soft materials,[210] they tend to be quite susceptible to streaking artifacts and blurring in the direction of the missing angular range. In recent years, similar CS algorithms to those discussed previously have been applied to retrieve the optimal undersampled dataset. Through non-linear compressive sensing electron tomography (CS-ET) algorithms, such as total variation minimization (TVM), beta process factor analysis, or 3D wavelet inpainting,[211–214] promising results have been demonstrated. These algorithms have been able to effectively inpaint the missing angular range and reduce the presence of blurring artifacts.[211,212,215–217] Additionally, these methods have proven to deliver high fidelity reconstructions with greater definition from structures such as nanoparticles, than those constructed using traditional reconstruction techniques such as WBP or SIRT, while requiring fewer projections.[216] This, of course, is quite attractive due to the beam sensitive nature of many soft materials. As a result, these algorithms offer another route in addition to traditional cryo-tomography for preserving HSI.[218,219]

Additionally, the sampling strategy itself can be varied by continuously rotating the sample in controlled rotational tomography (CORT) to create a sparsely sampled projection. Using CORT in conjunction with aforementioned CS-ET techniques, Li et al. were able to create reconstructions of beam-sensitive samples that were highly consistent with the ground truth structures.[220]

Alternatively, a serial defocus approach can provide 3D images of thicker samples, including hybrid nanocomposites.[221] Although ptychography is typically limited to ultra-thin samples, Gao et al. recently demonstrated that an inverse multislice ptychography method yields the complex 3D transmission function of a thick sample. This alternative is useful as the presence of multiple scattering events can lead to the captured signal violating the projection requirement.[222] Because ptychography is a low dose method, this approach allows for reconstruction of beam-sensitive structures with minimal loss of 3D resolution.[223]

Single particle analysis (SPA), a popular method in the cryo-EM community for analyzing and building 3D reconstructions of biological molecules, is yet another technique that may be valuable in the context of imaging HSI.[224–227] This technique involves imaging, classifying, and stitching together many identical molecules with different orientations using a class averaging approach. SPA can be performed with TEM or STEM, but the simpler contrast transfer function in STEM modes means fewer samples are needed for a reconstruction. This method is promising for understanding the interfacial structure in systems such as functionalized nanoparticles or MOFs, where identical geometries are readily accessible.[228,229] A similar construct combining the STEM-ADF and spectral signals has also received recent interest.[230,231]

4.2 *In Situ/Operando* STEM: Implications for soft/hybrid interfaces

The capability to detect a bevy of signals from highly localized volumes with microsecond temporal resolution makes STEM an incredibly useful tool for probing real time phenomena. During an *in*

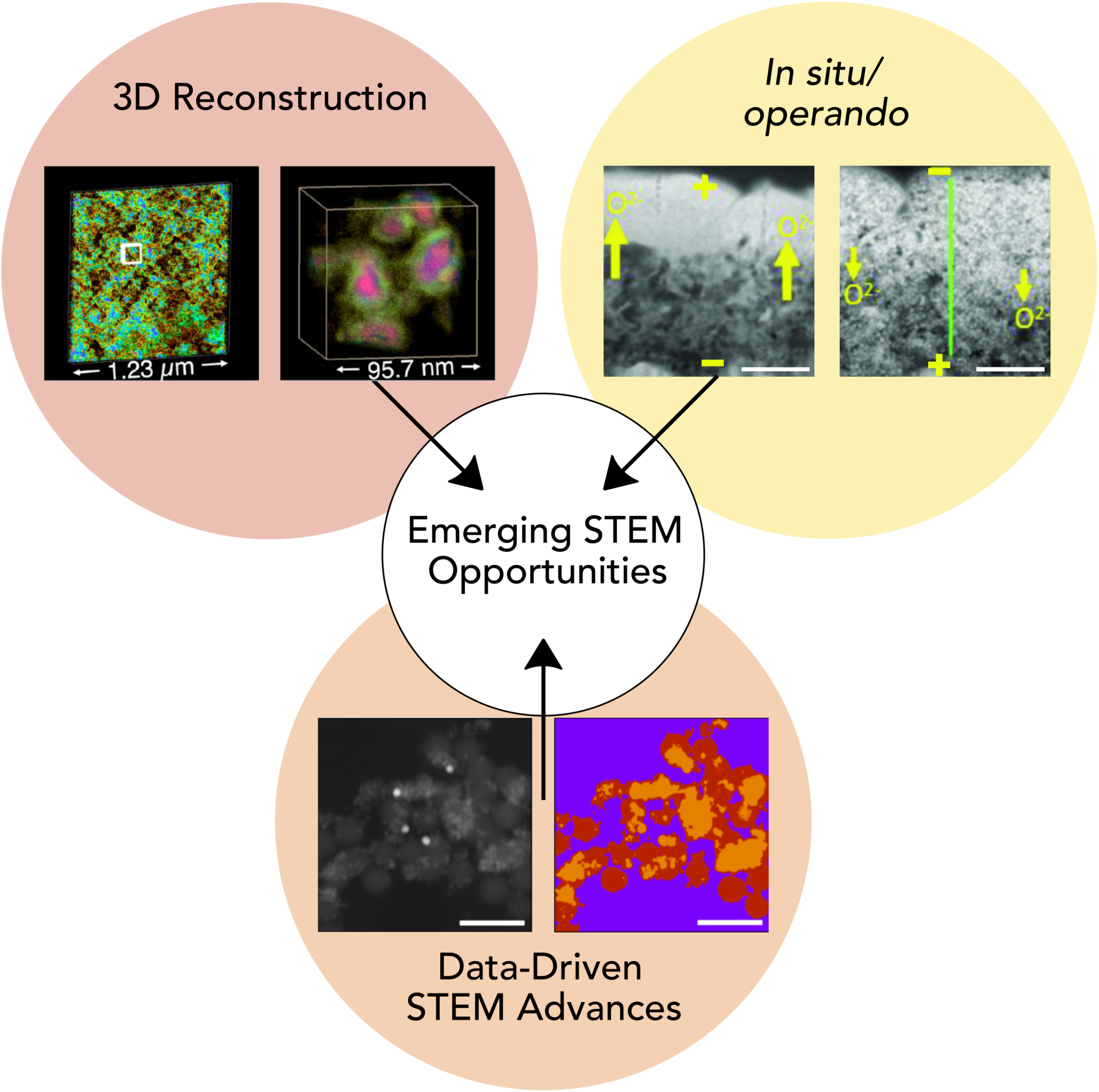

Figure 7: A subset of emerging opportunities in various parts of the STEM workflow: 3D reconstruction using tomographic methods, *in situ/operando* analysis, and advances in the data processing pipeline. Examples include quantitative, three-dimensional imaging of chromatin structure,,[232] observing electrically induced oxygen diffusion in inorganic/organic halide perovskites,[233] and development of machine learning algorithms for rapid classification of image features.

situ experiment, an external stimuli is applied to a system, and the cascading effects are monitored. It can be difficult to implement these experiments in practice, as the external stimulation mechanisms need to be compatible with the high vacuum environment and electron dose common to STEM. Recent advances in specialized holders have created opportunities for studying the impact of heating,[234] mechanical deformation,[235] optical stimulation,[233] electrical biasing[236,237] as well as the impact of liquid environments.[238,239]

This type of study is closely linked to the previous discussion of HSI, as changes often occur at the interfacial region between two materials. Moreover, the structural dynamics of interest are commonly accompanied by the migration of light atoms. There exist numerous papers demonstrating electrochemical diffusion of lithium and the structural evolution this induces at the electrode/electrolyte interface.[240,241] Similarly, optical stimulation can induce oxygen migration from the electron transport layer of the photovoltaic cell into the inorganic/organic halide perovskite active layer.[233] Oxygen evolution and reincorporation has also been found to play a key role in explaining hysteretic behavior in oxide-based ReRAM.[242] Additionally, in liquid cell STEM, the spatial resolution achievable is limited by the SNR, so achieving appreciable contrast from these light atoms takes on even greater importance.[238] Directly imaging these atoms with phase contrast techniques would simplify the resultant analysis and give greater insight into the presence of intermediary steps during this reaction process.

As *in situ* experiments commonly require extended electron exposures, DEDs and the dose-efficient methods described previously are quite valuable in limiting sample damage throughout this time frame. Through the high frame rates possible with DEDs as well as the ability to capture a series of sub-frames and align them together, it is possible to record dynamical processes, such as the deformation during tensile loading[243] or translational motion of a catalytic nanoparticle with millisecond temporal resolution and improved SNR.[244–246] Because information related to internal fields is captured in the phase component of the specimen transmission function, techniques such as differential phase contrast provide the ability to spatially characterize the in-plane electric or strain field responsible for the structural evolution.[243,247] Together these developments make it significantly easier to identify the impact of various stimuli on a nanoscale system.

4.3 Practical Data Acquisition, Processing, and Handling Advances to Improve the STEM Workflow

The rise of artificial intelligence ecosystems and associated machine learning algorithms has accelerated innovation in a wide variety of scientific disciplines including materials discovery.[248] Artificial intelligence has already begun to play an important role in material understanding through electron microscopy,[190,193,249–254] and we expect that in the coming years, the latest data analysis tools and techniques will revolutionize electron microscopy in ways that leave it better positioned to address major materials challenges. In this section, we discuss the potential impact that advances in this area such as real-time data processing, automated microscopy modules and improvements in data storage and processing workflows would have in the context of understanding HSI.

4.3.1 Automated Microscopy Modules for Streamlining Data Acquisition and Analysis

Just as other characterization methodologies such as x-ray crystallography have become increasingly automated in recent years,[255] the development of automated microscopy workstation would similarly streamline the data acquisition and analysis processes. We envision a paradigm where the microscopist would first image a few relevant and interesting regions, such as HSI, before leaning on a machine learning algorithm to explore an extensive worldwide microscopy database and procure the best course of action for further analysis. This would include defining a design space of possible microscope parameters that would be optimized for the particular tool through an auto-alignment procedure. It would also include identifying a set of ideal microscopy techniques for most effectively interrogating the sample of interest. This latter aspect could eliminate the implicit biases researchers may exhibit towards techniques and methodologies with which they are most familiar. By building a deeper connection between the human user and artificial intelligence, STEM is positioned to become a highly sought-after tool for probing and understanding intricate structure-property relationships.

4.3.2 Real-time Processing of STEM Data to Obtain Optimal Datasets

While the current workflow for constructing STEM phase contrast images from 4D-STEM datasets provides a high level of understanding of interfacial features, these methods often requires substantial offline processing time. Beyond practical value associated with reducing acquisition and analysis time, having real-time data processing, on-the-fly imaging allows for acquisition of better datasets. This construct would allow microscopists to more directly find optimal experimental conditions and regions of interest. The imaging techniques discussed here each have different sets of ideal conditions to enhance information transfer. With conventional techniques such as BF and ADF, these ideal conditions for information transfer are more readily identifiable than with phase techniques such as DPC or ptychography. The recent advent of detectors with live processing modules will allow for real-time processing of various phase contrast techniques.[256,257] This type of processing couples nicely with the automated engine discussed in the previous section to dynamically adjust to unexpected observations during a single microscope session.

4.3.3 Standardized Framework for Microscopy Data Management and Processing

Finally, a standardized approach based on the FAIR (Findable, Accessible, Interoperable, Reusable) guidelines for storing large datasets can dramatically accelerate materials understanding.[258] A standardized naming scheme can avoid headaches for the microscopist following a completed session and is valuable in helping computational algorithms draw trends between sample properties and experimental conditions.[259]

Accessing microscopy data is also a challenge as the sheer volume of generated data makes USB hard drives an impractical storage solution. Even cloud storage services may be impractical depending on the data transfer rate provided for transporting files from the acquisition computer to the cloud. One potential solution would be to create a centralized storage location within a local high-performance computing cluster that users would be able to access for subsequent analysis.[260]

The captured data can be made more interoperable through continued development of open-source scripts and applications for processing data. These tools can enhance the scientific accuracy of analysis as the user is privy to all data processing steps. Although there exist a variety of applications for performing particular analytical routines, we hope to see a continued development of computational ecosystems such as py4dSTEM,[261] pyXEM,[262] LiberTEM,,[263] pycroscopy,[264] pixStem[265] and hyperspy,,[266] etc. that serve as "one-stop shops" compatible with high performance computing clusters for streamlining analysis. The acceptance of open, hierarchical data formats that allow access to data subsets without having to store the entire dataset in RAM and support compression, such as the sparse HDF5 format, would increase interoperability as well.

Finally, data reusability requires microscopists to publish experimental datasets in repositories and is a key step to enable an automated microscopy engine. Moreover, it serves as a way for the field-at-large to perform quality control and maintain scientific integrity beyond traditional peer review.

5 Summary

Hybrid composites are a compelling class of materials offering considerable opportunity across a wide array of applications. Moreover, to facilitate further development in this field, it is crucial to understand the chemical and physical properties of these composites, especially at their interfaces. In this article, we have discussed the challenges associated with achieving sufficient image contrast in STEM, while preserving structural integrity, when analyzing the interfacial regions between hard and soft components. Enabled by recent advances, we have identified a number of solutions for mitigating these concerns and attaining a nano or atomic-level understanding of these interfaces. Furthermore, by combining these STEM solutions with tomography and *in situ/in operando* methods, rich structure and property information is realizable as well. As such, the multimodality of STEM represents a powerful method for understanding and enhancing the functionality and performance of this emerging class of composite materials.

Data availability

The raw/processed data required to reproduce these findings cannot be shared at this time due to technical or time limitations.

References

(1) Glimcher, M. J. Bone: Nature of the Calcium Phosphate Crystals and Cellular, Structural, and Physical Chemical Mechanisms in Their Formation. *Med. Mineraology and Geochem.* **2006**, *64*, 223–282.

(2) Hing, K. A. Bone Repair in the Twenty-First Century: Biology, Chemistry or Engineering? *Philos. Trans. R. Soc., A* **2004**, *362*, 2821–50.

(3) Lin, C. P.; Douglas, W. H.; Erlandsen, S. L. Scanning Electron Microscopy of Type I Collagen at the Dentin-Enamel Junction of Human Teeth. *J. Histochem. Cytochem.* **1993**, *41*, 381–8.

(4) Marshall, S. J.; Balooch, M.; Habelitz, S.; Balooch, G.; Gallagher, R.; Marshall, G. W. The Dentin-Enamel Junction - A Natural, Multilevel Interface. *J. Eur. Ceram. Soc.* **2003**, *23*, 2897–2904.

(5) DeRocher, K. A.; Smeets, P. J.; Goodge, B. H.; Zachman, M. J.; Balachandran, P. V.; Stegbauer, L.; Cohen, M. J.; Gordon, L. M.; Rondinelli, J. M.; Kourkoutis, L. F.; Joester, D. Chemical Gradients in Human Enamel Crystallites. *Nature* **2020**, *583*, 66–71.

(6) Li, X. D.; Chang, W. C.; Chao, Y. J.; Wang, R. Z.; Chang, M. Nanoscale Structural and Mechanical Characterization of a Natural Nanocomposite Material: The Shell of Red Abalone. *Nano Lett.* **2004**, *4*, 613–617.

(7) Li, X.; Xu, Z. H.; Wang, R. In Situ Observation of Nanograin Rotation and Deformation in Nacre. *Nano Lett.* **2006**, *6*, 2301–4.

(8) Mittal, G.; Rhee, K. Y.; Miskovic-Stankovic, V.; Hui, D. Reinforcements in Multi-Scale Polymer Composites: Processing, Properties, and Applications. *Composites, Part B* **2018**, *138*, 122–139.

(9) Asl, M. S.; Nayebi, B.; Ahmadi, Z.; Zamharir, M. J.; Shokouhimehr, M. Effects of Carbon Additives on the Properties of ZrB_2-Based Composites: A Review. *Ceram. Int.* **2018**, *44*, 7334–7348.

(10) Saha, K.; Agasti, S. S.; Kim, C.; Li, X.; Rotello, V. M. Gold Nanoparticles in Chemical and Biological Sensing. *Chem. Rev.* **2012**, *112*, 2739–79.

(11) Dreaden, E. C.; Alkilany, A. M.; Huang, X.; Murphy, C. J.; El-Sayed, M. A. The Golden Age: Gold Nanoparticles for Biomedicine. *Chem. Soc. Rev.* **2012**, *41*, 2740–2779.

(12) Lin, Q. Y.; Mason, J. A.; Li, Z.; Zhou, W.; O'Brien, M. N.; Brown, K. A.; Jones, M. R.; Butun, S.; Lee, B.; Dravid, V. P.; Aydin, K.; Mirkin, C. A. Building Superlattices From Individual Nanoparticles via Template-Confined DNA-Mediated Assembly. *Science* **2018**, *359*, 669–672.

(13) Macfarlane, R. J.; Lee, B.; Jones, M. R.; Harris, N.; Schatz, G. C.; Mirkin, C. A. Nanoparticle Superlattice Engineering With DNA. *Science* **2011**, *334*, 204–8.

(14) Nandwana, V.; Huang, W.; Li, Y.; Dravid, V. P. One-Pot Green Synthesis of Fe_3O_4/MoS_2 0d/2d Nanocomposites and Their Application in Noninvasive Point-Of-Care Glucose Diagnostics. *ACS App. Nano Mater.* **2018**, *1*, 1949–1958.

(15) Yang, Q.; Xu, Q.; Yu, S. H.; Jiang, H. L. Pd Nanocubes@ZIF-8: Integration of Plasmon-Driven Photothermal Conversion With a Metal-Organic Framework for Efficient and Selective Catalysis. *Angew. Chem., Int. Ed. Engl.* **2016**, *55*, 3685–9.

(16) Kuo, C. H.; Tang, Y.; Chou, L. Y.; Sneed, B. T.; Brodsky, C. N.; Zhao, Z.; Tsung, C. K. Yolk-Shell Nanocrystal@ZIF-8 Nanostructures for Gas-Phase Heterogeneous Catalysis With Selectivity Control. *J. Am. Chem. Soc.* **2012**, *134*, 14345–8.

(17) Lu, G. et al. Imparting Functionality to a Metal-Organic Framework Material by Controlled Nanoparticle Encapsulation. *Nat. Chem.* **2012**, *4*, 310–6.

(18) Chen, S.; Zhu, J. W.; Wu, X. D.; Han, Q. F.; Wang, X. Graphene Oxide-MnO_2 Nanocomposites for Supercapacitors. *ACS Nano* **2010**, *4*, 2822–2830.

(19) Gilman, J. W.; Jackson, C. L.; Morgan, A. B.; Harris, R.; Manias, E.; Giannelis, E. P.; Wuthenow, M.; Hilton, D.; Phillips, S. H. Flammability Properties of Polymer-Layered-Silicate Nanocomposites. Polypropylene and Polystyrene Nanocomposites. *Chem. Mater.* **2000**, *12*, 1866–1873.

(20) Zhang, X. Y.; Li, H. P.; Cui, X. L.; Lin, Y. H. Graphene/TiO_2 Nanocomposites: Synthesis, Characterization and Application in Hydrogen Evolution From Water Photocatalytic Splitting. *J. Mater. Chem.* **2010**, *20*, 2801–2806.

(21) Jia, L.; Wang, D. H.; Huang, Y. X.; Xu, A. W.; Yu, H. Q. Highly Durable N-Doped Graphene/CdS Nanocomposites With Enhanced Photocatalytic Hydrogen Evolution From Water Under Visible Light Irradiation. *J. Phys. Chem. C* **2011**, *115*, 11466–11473.

(22) Nandwana, V.; Ribet, S. M.; Reis, R. D.; Kuang, Y.; More, Y.; Dravid, V. P. OHM Sponge: A Versatile, Efficient, and Ecofriendly Environmental Remediation Platform. *Ind. Eng. Chem. Res.* **2020**, *59*, 10945–10954.

(23) Li, Y.; Majewski, M. B.; Islam, S. M.; Hao, S.; Murthy, A. A.; DiStefano, J. G.; Hanson, E. D.; Xu, Y.; Wolverton, C.; Kanatzidis, M. G.; Wasielewski, M. R.; Chen, X.; Dravid, V. P. Morphological Engineering of Winged Au@MoS_2 Heterostructures for Electrocatalytic Hydrogen Evolution. *Nano Lett.* **2018**, *18*, 7104–7110.

(24) Li, Y.; DiStefano, J. G.; Murthy, A. A.; Cain, J. D.; Hanson, E. D.; Li, Q.; Castro, F. C.; Chen, X.; Dravid, V. P. Superior Plasmonic Photodetectors Based on Au@MoS_2 Core-Shell Heterostructures. *ACS Nano* **2017**, *11*, 10321–10329.

(25) Wang, D. W.; Li, F.; Zhao, J.; Ren, W.; Chen, Z. G.; Tan, J.; Wu, Z. S.; Gentle, I.; Lu, G. Q.; Cheng, H. M. Fabrication of Graphene/Polyaniline Composite Paper via in Situ

Anodic Electropolymerization for High-Performance Flexible Electrode. *ACS Nano* **2009**, *3*, 1745–52.

(26) Kulbak, M.; Cahen, D.; Hodes, G. How Important Is the Organic Part of Lead Halide Perovskite Photovoltaic Cells? Efficient $CsPbBr_3$ Cells. *J. Phys. Chem. Lett.* **2015**, *6*, 2452–6.

(27) Gong, S.; Yap, L. W.; Zhu, B.; Cheng, W. Multiscale Soft-Hard Interface Design for Flexible Hybrid Electronics. *Adv. Mater.* **2020**, *32*, e1902278.

(28) Yang, R.; Chen, G.; Dresselhaus, M. S. Thermal Conductivity Modeling of Core-Shell and Tubular Nanowires. *Nano Lett.* **2005**, *5*, 1111–5.

(29) Ciprari, D.; Jacob, K.; Tannenbaum, R. Characterization of Polymer Nanocomposite Interphase and Its Impact on Mechanical Properties. *Macromolecules* **2006**, *39*, 6565–6573.

(30) Wang, Y.; Zhang, Y.; Zhao, H.; Li, X.; Huang, Y.; Schadler, L. S.; Chen, W.; Brinson, L. C. Identifying Interphase Properties in Polymer Nanocomposites Using Adaptive Optimization. *Compos. Sci. Technol.* **2018**, *162*, 146–155.

(31) Zhang, H.; Zhang, Z.; Friedrich, K.; Eger, C. Property Improvements of in Situ Epoxy Nanocomposites With Reduced Interparticle Distance at High Nanosilica Content. *Acta Mater.* **2006**, *54*, 1833–1842.

(32) Zhandarov, S.; Mader, E. Characterization of Fiber/Matrix Interface Strength: Applicability of Different Tests, Approaches and Parameters. *Compos. Sci. Technol.* **2005**, *65*, 149–160.

(33) Hage, F. S.; Kepaptsoglou, D. M.; Ramasse, Q. M.; Allen, L. J. Phonon Spectroscopy at Atomic Resolution. *Phys. Rev. Lett.* **2019**, *122*, 016103.

(34) Hage, F. S.; Nicholls, R. J.; Yates, J. R.; McCulloch, D. G.; Lovejoy, T. C.; Dellby, N.; Krivanek, O. L.; Refson, K.; Ramasse, Q. M. Nanoscale Momentum-Resolved Vibrational Spectroscopy. *Sci. Adv.* **2018**, *4*, eaar7495.

(35) Krivanek, O. L.; Chisholm, M. F.; Nicolosi, V.; Pennycook, T. J.; Corbin, G. J.; Dellby, N.; Murfitt, M. F.; Own, C. S.; Szilagyi, Z. S.; Oxley, M. P.; Pantelides, S. T.; Pennycook, S. J. Atom-By-Atom Structural and Chemical Analysis by Annular Dark-Field Electron Microscopy. *Nature* **2010**, *464*, 571–574.

(36) Yu, X. Z.; Onose, Y.; Kanazawa, N.; Park, J. H.; Han, J. H.; Matsui, Y.; Nagaosa, N.; Tokura, Y. Real-Space Observation of a Two-Dimensional Skyrmion Crystal. *Nature* **2010**, *465*, 901–904.

(37) Scholl, J. A.; Koh, A. L.; Dionne, J. A. Quantum Plasmon Resonances of Individual Metallic Nanoparticles. *Nature* **2012**, *483*, 421–7.

(38) Meyer, J. C.; Kurasch, S.; Park, H. J.; Skakalova, V.; Kunzel, D.; Gross, A.; Chuvilin, A.; Algara-Siller, G.; Roth, S.; Iwasaki, T.; Starke, U.; Smet, J. H.; Kaiser, U. Experimental Analysis of Charge Redistribution Due to Chemical Bonding by High-Resolution Transmission Electron Microscopy. *Nat. Mater.* **2011**, *10*, 209–15.

(39) Wang, F. et al. Conversion Reaction Mechanisms in Lithium Ion Batteries: Study of the Binary Metal Fluoride Electrodes. *J. Am. Chem. Soc.* **2011**, *133*, 18828–36.

(40) Yin, P.; Yao, T.; Wu, Y.; Zheng, L.; Lin, Y.; Liu, W.; Ju, H.; Zhu, J.; Hong, X.; Deng, Z.; Zhou, G.; Wei, S.; Li, Y. Single Cobalt Atoms With Precise N-Coordination as Superior Oxygen Reduction Reaction Catalysts. *Angew. Chem., Int. Ed. Engl.* **2016**, *55*, 10800–5.

(41) Mayer, J.; Giannuzzi, L. A.; Kamino, T.; Michael, J. TEM Sample Preparation and FIB-Induced Damage. *MRS Bull.* **2007**, *32*, 400–407.

(42) Egerton, R. F. Radiation Damage to Organic and Inorganic Specimens in the TEM. *Micron* **2019**, *119*, 72–87.

(43) Egerton, R. F. Control of Radiation Damage in the TEM. *Ultramicroscopy* **2013**, *127*, 100–8.

(44) Zhang, D.; Zhu, Y.; Liu, L.; Ying, X.; Hsiung, C. E.; Sougrat, R.; Li, K.; Han, Y. Atomic-resolution transmission electron microscopy of electron beam-sensitive crystalline materials. *Science* **2018**, *359*, 675–679.

(45) Yu, Y.; Zhang, D.; Kisielowski, C.; Dou, L.; Kornienko, N.; Bekenstein, Y.; Wong, A. B.; Alivisatos, A. P.; Yang, P. Atomic Resolution Imaging of Halide Perovskites. *Nano Letters* **2016**, *16*, 7530–7535.

(46) Chen, Q.; Dwyer, C.; Sheng, G.; Zhu, C.; Li, X.; Zheng, C.; Zhu, Y. Imaging Beam-Sensitive Materials by Electron Microscopy. *Advanced Materials* **2020**, *32*, 1907619.

(47) Zhang, D.; Zhu, Y.; Liu, L.; Ying, X.; Hsiung, C.-E.; Sougrat, R.; Li, K.; Han, Y. Atomic-resolution transmission electron microscopy of electron beam–sensitive crystalline materials. *Science* **2018**, *359*, 675–679.

(48) Henderson, R. The Potential and Limitations of Neutrons, Electrons and X-Rays for Atomic Resolution Microscopy of Unstained Biological Molecules. *Q. Rev. Biophys.* **1995**, *28*, 171–93.

(49) Egerton, R. F.; Li, P.; Malac, M. Radiation Damage in the TEM and SEM. *Micron* **2004**, *35*, 399–409.

(50) Urban, K. Radiation-Induced Processes in Experiments Carried Out In-Situ in the High-Voltage Electron Microscope. *Phys. Status Solidi A* **1979**, *56*, 157–168.

(51) Erickson, H. P. Size and Shape of Protein Molecules at the Nanometer Level Determined by Sedimentation, Gel Filtration, and Electron Microscopy. *Biol. Proced. Online* **2009**, *11*, 32–51.

(52) Mikula, S.; Denk, W. High-Resolution Whole-Brain Staining for Electron Microscopic Circuit Reconstruction. *Nat. Methods* **2015**, *12*, 541–6.

(53) Mikula, S.; Binding, J.; Denk, W. Staining and Embedding the Whole Mouse Brain for Electron Microscopy. *Nat. Methods* **2012**, *9*, 1198–201.

(54) Li, X.; Mooney, P.; Zheng, S.; Booth, C. R.; Braunfeld, M. B.; Gubbens, S.; Agard, D. A.; Cheng, Y. Electron Counting and Beam-Induced Motion Correction Enable Near-Atomic-Resolution Single-Particle Cryo-Em. *Nat. Methods* **2013**, *10*, 584–90.

(55) Franken, L. E.; Grünewald, K.; Boekema, E. J.; Stuart, M. C. A Technical Introduction to Transmission Electron Microscopy for Soft-Matter: Imaging, Possibilities, Choices, and Technical Developments. *Small* **2020**, *16*, 1906198.

(56) Walls, A. C.; Tortorici, M. A.; Bosch, B. J.; Frenz, B.; Rottier, P. J. M.; DiMaio, F.; Rey, F. A.; Veesler, D. Cryo-Electron Microscopy Structure of a Coronavirus Spike Glycoprotein Trimer. *Nature* **2016**, *531*, 114–117.

(57) Zheng, S. Q.; Palovcak, E.; Armache, J. P.; Verba, K. A.; Cheng, Y.; Agard, D. A. MotionCor2: Anisotropic Correction of Beam-Induced Motion for Improved Cryo-Electron Microscopy. *Nat. Methods* **2017**, *14*, 331–332.

(58) Hujsak, K. A.; Roth, E. W.; Kellogg, W.; Li, Y.; Dravid, V. P. High Speed/Low Dose Analytical Electron Microscopy With Dynamic Sampling. *Micron* **2018**, *108*, 31–40.

(59) de Graaf, S.; Momand, J.; Mitterbauer, C.; Lazar, S.; Kooi, B. J. Resolving Hydrogen Atoms at Metal-Metal Hydride Interfaces. *Sci. Adv.* **2020**, *6*, eaay4312.

(60) Yang, H.; Rutte, R. N.; Jones, L.; Simson, M.; Sagawa, R.; Ryll, H.; Huth, M.; Pennycook, T. J.; Green, M. L.; Soltau, H.; Kondo, Y.; Davis, B. G.; Nellist, P. D. Simultaneous Atomic-Resolution Electron Ptychography and Z-Contrast Imaging of Light and Heavy Elements in Complex Nanostructures. *Nat. Commun.* **2016**, *7*, 12532.

(61) Ophus, C.; Ciston, J.; Pierce, J.; Harvey, T. R.; Chess, J.; McMorran, B. J.; Czarnik, C.; Rose, H. H.; Ercius, P. Efficient Linear Phase Contrast in Scanning Transmission Electron Microscopy With Matched Illumination and Detector Interferometry. *Nat. Commun.* **2016**, *7*, 10719.

(62) Wang, G. L.; Murray, R. W. Controlled Assembly of Monolayer-Protected Gold Clusters by Dissolved DNA. *Nano Lett.* **2004**, *4*, 95–101.

(63) Kumar, A.; Pattarkine, M.; Bhadbhade, M.; Mandale, A. B.; Ganesh, K. N.; Datar, S. S.; Dharmadhikari, C. V.; Sastry, M. Linear Superclusters of Colloidal Gold Particles by Electrostatic Assembly on DNA Templates. *Adv. Mater.* **2001**, *13*, 341–344.

(64) Que, E. L.; Duncan, F. E.; Bayer, A. R.; Philips, S. J.; Roth, E. W.; Bleher, R.; Gleber, S. C.; Vogt, S.; Woodruff, T. K.; O'Halloran, T. V. Zinc Sparks Induce Physiochemical Changes in the Egg Zona Pellucida That Prevent Polyspermy. *Integr. Biol.* **2017**, *9*, 135–144.

(65) Choudhuri, K.; Llodrá, J.; Roth, E. W.; Tsai, J.; Gordo, S.; Wucherpfennig, K. W.; Kam, L. C.; Stokes, D. L.; Dustin, M. L. Polarized Release of T-Cell-Receptor-Enriched Microvesicles at the Immunological Synapse. *Nature* **2014**, *507*, 118–123.

(66) Zhang, X.; Hao, S.; Tan, G.; Hu, X.; Roth, E. W.; Kanatzidis, M. G.; Wolverton, C.; Dravid, V. P. Ion Beam Induced Artifacts in Lead-Based Chalcogenides. *Microsc. Microanal.* **2019**, *25*, 831–839.

(67) Zhang, F.; Hu, X.; Roth, E. W.; Kim, Y.; Nguyen, S. T. Template-Assisted, Seed-Mediated Synthesis of Hierarchically Mesoporous Core–Shell UiO-66: Enhancing Adsorption Capacity and Catalytic Activity Through Iterative Growth. *Chem. Mater.* **2020**, *32*, 4292–4302.

(68) Kennedy, N. W.; Hershewe, J. M.; Nichols, T. M.; Roth, E. W.; Wilke, C. D.; Mills, C. E.; Jewett, M. C.; Tullman-Ercek, D. Apparent Size and Morphology of Bacterial Microcompartments Varies With Technique. *PLoS One* **2020**, *15*, e0226395.

(69) Wang, S.; Park, S. S.; Buru, C. T.; Lin, H.; Chen, P. C.; Roth, E. W.; Farha, O. K.; Mirkin, C. A. Colloidal Crystal Engineering With Metal-Organic Framework Nanoparticles and DNA. *Nat. Commun.* **2020**, *11*, 2495.

(70) Thomas, S. A.; Rodby, K. E.; Roth, E. W.; Wu, J.; Gaillard, J. F. Spectroscopic and Microscopic Evidence of Biomediated HgS Species Formation From Hg(II)-Cysteine Complexes: Implications for Hg(II) Bioavailability. *Environ. Sci. Technol.* **2018**, *52*, 10030–10039.

(71) Studer, D.; Gnaegi, H. Minimal Compression of Ultrathin Sections with use of an Oscillating Diamond Knife. *J. Microsc.* **2000**, *197*, 94—100.

(72) Ayache, J.; Beaunier, L.; Boumendil, J.; Ehret, G.; Laub, D. *Sample preparation handbook for transmission electron microscopy: techniques*; Springer Science & Business Media, 2010; Vol. 2.

(73) Wu, Q.; Li, M.; Gu, Y. Z.; Wang, S. K.; Zhang, Z. G. Imaging the Interphase of Carbon Fiber Composites Using Transmission Electron Microscopy: Preparations by Focused Ion Beam, Ion Beam Etching, and Ultramicrotomy. *Chin. J. Aeronaut.* **2015**, *28*, 1529–1538.

(74) Mucha, H.; Kato, T.; Arai, S.; Saka, H.; Kuroda, K.; Wielage, B. Focused Ion Beam Preparation Techniques Dedicated for the Fabrication of TEM Lamellae of Fibre-Reinforced Composites. *J. Electron. Microsc.* **2005**, *54*, 43–9.

(75) Huson, M. G.; Church, J. S.; Hillbrick, L. K.; Woodhead, A. L.; Sridhar, M.; Van De Meene, A. M. L. Focused Ion Beam Milling of Carbon Fibres. *Mater. Chem. Phys.* **2015**, *168*, 193–200.

(76) Kim, S.; Dravid, V. P. Focused Ion Beam Sample Preparation of Continuous Fibre-Reinforced Ceramic Composite Specimens for Transmission Electron Microscopy. *J. Microsc.* **2000**, *198*, 124–133.

(77) Giannuzzi, L. A.; Phifer, D.; Giannuzzi, N. J.; Capuano, M. J. Two-Dimensional and 3-Dimensional Analysis of Bone/Dental Implant Interfaces With the Use of Focused Ion Beam and Electron Microscopy. *Int. J. Oral Surg.* **2007**, *65*, 737–747.

(78) Younis, S.; Kauffmann, Y.; Bloch, L.; Zolotoyabko, E. Inhomogeneity of Nacre Lamellae on the Nanometer Length Scale. *Cryst. Growth Des.* **2012**, *12*, 4574–4579.

(79) Supasai, T.; Henjongchom, N.; Tang, I. M.; Deng, F.; Rujisamphan, N. Compact Nanostructured TiO2 Deposited by Aerosol Spray Pyrolysis for the Hole-Blocking Layer in a CH3NH3PbI3 Perovskite Solar Cell. *Sol. Energy* **2016**, *136*, 515–524.

(80) Lu, Y.; Ding, Y.; Qiu, Y.; Cai, K.; Yao, Q.; Song, H.; Tong, L.; He, J.; Chen, L. Good Performance and Flexible PEDOT:PSS/Cu2Se Nanowire Thermoelectric Composite Films. *ACS Appl. Mater. Interfaces* **2019**, *11*, 12819–12829.

(81) Grandfield, K.; Palmquist, A.; Engqvist, H. Three-Dimensional Structure of Laser-Modified Ti6Al4V and Bone Interface Revealed With STEM Tomography. *Ultramicroscopy* **2013**, *127*, 48–52.

(82) Zhong, X. L.; Schilling, S.; Zaluzec, N. J.; Burke, M. G. Sample Preparation Methodologies for in Situ Liquid and Gaseous Cell Analytical Transmission Electron Microscopy of Electropolished Specimens. *Microsc. Microanal.* **2016**, *22*, 1350–1359.

(83) Mayer, J.; Giannuzzi, L. A.; Kamino, T.; Michael, J. TEM Sample Preparation and FIB-induced Damage. *MRS Bull.* **2007**, *32*, 400–407.

(84) Phaneuf, M. W. Applications of Focused Ion Beam Microscopy to Materials Science Specimens. *Micron* **1999**, *30*, 277–288.

(85) Giannuzzi, L. A.; Stevie, F. A. A Review of Focused Ion Beam Milling Techniques for TEM Specimen Preparation. *Micron* **1999**, *30*, 197–204.

(86) Mahamid, J.; Schampers, R.; Persoon, H.; Hyman, A. A.; Baumeister, W.; Plitzko, J. M. A Focused Ion Beam Milling and Lift-Out Approach for Site-Specific Preparation of Frozen-Hydrated Lamellas From Multicellular Organisms. *J. Struct. Biol.* **2015**, *192*, 262–9.

(87) Rubino, S.; Akhtar, S.; Melin, P.; Searle, A.; Spellward, P.; Leifer, K. A Site-Specific Focused-Ion-Beam Lift-Out Method for Cryo Transmission Electron Microscopy. *J. Struct. Biol.* **2012**, *180*, 572–6.

(88) Zachman, M. J.; Tu, Z.; Choudhury, S.; Archer, L. A.; Kourkoutis, L. F. Cryo-Stem Mapping of Solid–liquid Interfaces and Dendrites in Lithium-Metal Batteries. *Nature* **2018**, *560*, 345–349.

(89) Huang, Z. Combining Ar Ion Milling With FIB Lift-Out Techniques to Prepare High Quality Site-Specific TEM Samples. *J. Microsc.* **2004**, *215*, 219–23.

(90) Tracy, B. M.; Doremus, R. H. Direct Electron Microscopy Studies of the Bone-Hydroxylapatite Interface. *J. Biomed. Mater. Res.* **1984**, *18*, 719–26.

(91) Zheng, Y.; Williams, R. E.; Nag, S.; Banerjee, R.; Fraser, H. L.; Banerjee, D. The effect of alloy composition on instabilities in the β phase of titanium alloys. *Scripta Materialia* **2016**, *116*, 49–52.

(92) Du, C.; Hoefnagels, J. P. M.; Bergers, L. I. J. C.; Geers, M. G. D. A Uni-Axial Nano-Displacement Micro-Tensile Test of Individual Constituents From Bulk Material. *Experimental Mechanics* **2017**, *57*, 1249–1263.

(93) Vermeij, T.; Plancher, E.; Tasan, C. C. Preventing Damage and Redeposition During Focused Ion Beam Milling: The "Umbrella" Method. *Ultramicroscopy* **2018**, *186*, 35–41.

(94) Wang, Z.; Hryc, C. F.; Bammes, B.; Afonine, P. V.; Jakana, J.; Chen, D. H.; Liu, X.; Baker, M. L.; Kao, C.; Ludtke, S. J.; Schmid, M. F.; Adams, P. D.; Chiu, W. An Atomic Model of Brome Mosaic Virus Using Direct Electron Detection and Real-Space Optimization. *Nat. Commun.* **2014**, *5*, 4808.

(95) Park, J.; Elmlund, H.; Ercius, P.; Yuk, J. M.; Limmer, D. T.; Chen, Q.; Kim, K.; Han, S. H.; Weitz, D. A.; Zettl, A.; Alivisatos, A. P. Nanoparticle Imaging. 3D Structure of Individual Nanocrystals in Solution by Electron Microscopy. *Science* **2015**, *349*, 290–5.

(96) Battaglia, M.; Contarato, D.; Denes, P.; Giubilato, P. Cluster Imaging With a Direct Detection CMOS Pixel Sensor in Transmission Electron Microscopy. *Nucl. Instrum. Methods Phys. Res., Sect. A* **2009**, *608*, 363–365.

(97) McMullan, G.; Chen, S.; Henderson, R.; Faruqi, A. R. Detective Quantum Efficiency of Electron Area Detectors in Electron Microscopy. *Ultramicroscopy* **2009**, *109*, 1126–43.

(98) McMullan, G.; Faruqi, A. R.; Clare, D.; Henderson, R. Comparison of Optimal Performance at 300keV of Three Direct Electron Detectors for Use in Low Dose Electron Microscopy. *Ultramicroscopy* **2014**, *147*, 156–63.

(99) Zhu, Y.; Ciston, J.; Zheng, B.; Miao, X.; Czarnik, C.; Pan, Y.; Sougrat, R.; Lai, Z.; Hsiung, C. E.; Yao, K.; Pinnau, I.; Pan, M.; Han, Y. Unravelling Surface and Interfacial Structures of a Metal-Organic Framework by Transmission Electron Microscopy. *Nat. Mater.* **2017**, *16*, 532–536.

(100) Nam, K. W.; Park, S. S.; Dos Reis, R.; Dravid, V. P.; Kim, H.; Mirkin, C. A.; Stoddart, J. F. Conductive 2D Metal-Organic Framework for High-Performance Cathodes in Aqueous Rechargeable Zinc Batteries. *Nat. Commun.* **2019**, *10*, 4948.

(101) Zhang, D.; Zhu, Y.; Liu, L.; Ying, X.; Hsiung, C. E.; Sougrat, R.; Li, K.; Han, Y. Atomic-Resolution Transmission Electron Microscopy of Electron Beam-Sensitive Crystalline Materials. *Science* **2018**, *359*, 675–679.

(102) Ophus, C.; Ercius, P.; Sarahan, M.; Czarnik, C.; Ciston, J. Recording and Using 4d-Stem Datasets in Materials Science. *Microsc. Microanal.* **2014**, *20*, 62–63.

(103) Ophus, C. Four-Dimensional Scanning Transmission Electron Microscopy (4d-Stem): From Scanning Nanodiffraction to Ptychography and Beyond. *Microsc. Microanal.* **2019**, *25*, 563–582.

(104) Plotkin-Swing, B.; Corbin, G. J.; De Carlo, S.; Dellby, N.; Hoermann, C.; Hoffman, M. V.; Lovejoy, T. C.; Meyer, C. E.; Mittelberger, A.; Pantelic, R.; Piazza, L.; Krivanek, O. L. Hybrid pixel direct detector for electron energy loss spectroscopy. *Ultramicroscopy* **2020**, *217*, 113067.

(105) Jiang, Y.; Chen, Z.; Han, Y.; Deb, P.; Gao, H.; Xie, S.; Purohit, P.; Tate, M. W.; Park, J.; Gruner, S. M.; Elser, V.; Muller, D. A. Electron Ptychography of 2D Materials to Deep Sub-Angstrom Resolution. *Nature* **2018**, *559*, 343–349.

(106) Carter, C. B.; Williams, D. B. *Transmission electron microscopy: Diffraction, imaging, and spectrometry*; Springer, 2016.

(107) Wang, Z. W.; Li, Z. Y.; Park, S. J.; Abdela, A.; Tang, D.; Palmer, R. E. Quantitative Z-Contrast Imaging in the Scanning Transmission Electron Microscope With Size-Selected Clusters. *Phys. Rev. B* **2011**, *84*, 073408.

(108) Nellist, P.; Pennycook, S. The principles and interpretation of annular dark-field Z-contrast imaging. *Advances in imaging and electron physics* **2000**, *113*, 147–203.

(109) Kirkland, E. J. *Advanced Computing in Electron Microscopy*; Springer, 2020.

(110) Yucelen, E.; Lazic, I.; Bosch, E. G. T. Phase Contrast Scanning Transmission Electron Microscopy Imaging of Light and Heavy Atoms at the Limit of Contrast and Resolution. *Sci. Rep.* **2018**, *8*, 2676.

(111) Cowley, J. M. Scanning Transmission Electron Microscopy of Thin Specimens. *Ultramicroscopy* **1976**, *2*, 3–16.

(112) Zeltmann, S. E.; Muller, A.; Bustillo, K. C.; Savitzky, B.; Hughes, L.; Minor, A. M.; Ophus, C. Patterned Probes for High Precision 4d-Stem Bragg Measurements. *Ultramicroscopy* **2020**, *209*, 112890.

(113) Pekin, T. C.; Gammer, C.; Ciston, J.; Minor, A. M.; Ophus, C. Optimizing Disk Registration Algorithms for Nanobeam Electron Diffraction Strain Mapping. *Ultramicroscopy* **2017**, *176*, 170–176.

(114) Hong, X.; Zeltmann, S. E.; Savitzky, B. H.; DaCosta, L. R.; Mueller, A.; Minor, A. M.; Bustillo, K.; Ophus, C. Multibeam Electron Diffraction. 2020.

(115) Rose, H. Phase Contrast in Scanning Electron Microscopy. *Optik* **1974**, *39*, 416–436.

(116) Findlay, S. D.; Shibata, N.; Sawada, H.; Okunishi, E.; Kondo, Y.; Yamamoto, T.; Ikuhara, Y. Robust Atomic Resolution Imaging of Light Elements Using Scanning Transmission Electron Microscopy. *App. Phys. Lett.* **2009**, *95*, 191913.

(117) Findlay, S. D.; Huang, R.; Ishikawa, R.; Shibata, N.; Ikuhara, Y. Direct Visualization of Lithium via Annular Bright Field Scanning Transmission Electron Microscopy: A Review. *Microscopy (Oxford, U. K.)* **2017**, *66*, 3–14.

(118) Okunishi, E.; Ishikawa, I.; Sawada, H.; Hosokawa, F.; Hori, M.; Kondo, Y. Visualization of Light Elements at Ultrahigh Resolution by STEM Annular Bright Field Microscopy. *Microsc. Microanal.* **2009**, *15*, 164–165.

(119) Findlay, S. D.; Shibata, N.; Sawada, H.; Okunishi, E.; Kondo, Y.; Ikuhara, Y. Dynamics of Annular Bright Field Imaging in Scanning Transmission Electron Microscopy. *Ultramicroscopy* **2010**, *110*, 903–23.

(120) Gao, P.; Kumamoto, A.; Ishikawa, R.; Lugg, N.; Shibata, N.; Ikuhara, Y. Picometer-Scale Atom Position Analysis in Annular Bright-Field STEM Imaging. *Ultramicroscopy* **2018**, *184*, 177–187.

(121) Ishikawa, R.; Okunishi, E.; Sawada, H.; Kondo, Y.; Hosokawa, F.; Abe, E. Direct Imaging of Hydrogen-Atom Columns in a Crystal by Annular Bright-Field Electron Microscopy. *Nat. Mater.* **2011**, *10*, 278–81.

(122) Oshima, Y.; Lee, S.; Takayanagi, K. Visualization of Lithium Ions by Annular Bright Field Imaging. *Microscopy (Oxford, U. K.)* **2017**, *66*, 15–24.

(123) Findlay, S. D.; Huang, R.; Ishikawa, R.; Shibata, N.; Ikuhara, Y. Direct Visualization of Lithium via Annular Bright Field Scanning Transmission Electron Microscopy: A Review. *Microscopy (Oxford, U. K.)* **2017**, *66*, 3–14.

(124) Tong, Y. X.; Zhang, Q. H.; Gu, L. Scanning Transmission Electron Microscopy: A Review of High Angle Annular Dark Field and Annular Bright Field Imaging and Applications in Lithium-Ion Batteries. *Chin. Phys. B* **2018**, *27*, 066107.

(125) Lee, S.; Oshima, Y.; Hosono, E.; Zhou, H.; Takayanagi, K. Reversible Contrast in Focus Series of Annular Bright Field Images of a Crystalline LiMn2O4 Nanowire. *Ultramicroscopy* **2013**, *125*, 43–48.

(126) Gu, L.; Zhu, C.; Li, H.; Yu, Y.; Li, C.; Tsukimoto, S.; Maier, J.; Ikuhara, Y. Direct Observation of Lithium Staging in Partially Delithiated LiFePO4 at Atomic Resolution. *J. Am. Chem. Soc.* **2011**, *133*, 4661–3.

(127) Lai, W.-H.; Zhang, B.-W.; Hu, Z.; Qu, X.-M.; Jiang, Y.-X.; Wang, Y.-X.; Wang, J.-Z.; Liu, H. K.; Chou, S.-L. The Quasi-Pt-Allotrope Catalyst: Hollow PtCo@single-Atom Pt1 on

Nitrogen-Doped Carbon Toward Superior Oxygen Reduction. *Adv. Funct. Mater.* **2019**, *29*, 1807340.

(128) Ishikawa, R.; Okunishi, E.; Sawada, H.; Kondo, Y.; Hosokawa, F.; Abe, E. Direct Imaging of Hydrogen-Atom Columns in a Crystal by Annular Bright-Field Electron Microscopy. *Nat. Mater.* **2011**, *10*, 278–81.

(129) Zhou, D.; Müller-Caspary, K.; Sigle, W.; Krause, F. F.; Rosenauer, A.; van Aken, P. A. Sample tilt effects on atom column position determination in ABF–STEM imaging. *Ultramicroscopy* **2016**, *160*, 110–117.

(130) Ercius, P.; Muller, D. Incoherent Bright Field STEM for Imaging and Tomography of Ultra-Thick TEM Cross-sections. *Microscopy and Microanalysis* **2009**, *15*, 238–239.

(131) Ercius, P.; Weyland, M.; Muller, D. A.; Gignac, L. M. Three-dimensional imaging of nanovoids in copper interconnects using incoherent bright field tomography. *Applied Physics Letters* **2006**, *88*, 243116.

(132) Dekkers, N.; De Lang, H. Differential phase contrast in a STEM. *Optik* **1974**, *41*, 452–456.

(133) Waddell, E.; Chapman, J. Linear imaging of strong phase objects using asymmetrical detectors in STEM. *Optik* **1979**, *54*, 83–96.

(134) Lazić, I.; Bosch, E. G. T.; Lazar, S. Phase Contrast STEM for Thin Samples: Integrated Differential Phase Contrast. *Ultramicroscopy* **2016**, *160*, 265–280.

(135) Bosch, E. G. T.; Lazic, I.; Lazar, S. Integrated Differential Phase Contrast (iDPC) STEM: A New Atomic Resolution STEM Technique to Image All Elements Across the Periodic Table. *Microsc. Microanal.* **2016**, *22*, 306–307.

(136) Bak, J.; Bin Bae, H.; Chung, S. Y. Atomic-Scale Perturbation of Oxygen Octahedra via Surface Ion Exchange in Perovskite Nickelates Boosts Water Oxidation. *Nat. Commun.* **2019**, *10*, 2713.

(137) Yücelen, E.; Lazić, I.; Bosch, E. G. T. Phase Contrast Scanning Transmission Electron Microscopy Imaging of Light and Heavy Atoms at the Limit of Contrast and Resolution. *Sci. Rep.* **2018**, *8*, 2676.

(138) de Graaf, S.; Momand, J.; Mitterbauer, C.; Lazar, S.; Kooi, B. J. Resolving Hydrogen Atoms at Metal-Metal Hydride Interfaces. *Sci. Adv.* **2020**, *6*, eaay4312.

(139) Liu, L.; Lopez-Haro, M.; Lopes, C. W.; Li, C.; Concepcion, P.; Simonelli, L.; Calvino, J. J.; Corma, A. Regioselective Generation and Reactivity Control of Subnanometric Platinum Clusters in Zeolites for High-Temperature Catalysis. *Nat. Mater.* **2019**, *18*, 866–873.

(140) Carlsson, A.; Alexandrou, I.; Yücelen, E.; Bosch, E. G. T.; Lazić, I. Low Dose Imaging Using Simultaneous iDPC- And ADF-STEM for Beam Sensitive Crystalline Structures. *Microsc. Microanal.* **2018**, *24*, 122–123.

(141) Kosinov, N.; Hensen, E. J. M. Reactivity, Selectivity, and Stability of Zeolite-Based Catalysts for Methane Dehydroaromatization. *Adv. Mater.* **2020**, *n/a*, e2002565.

(142) Kumar, A.; Baker, J. N.; Bowes, P. C.; Cabral, M. J.; Zhang, S.; Dickey, E.; Irving, D. L.; LeBeau, J. M. Decoding the Complexities of Lead-Based Relaxor Ferroelectrics. 2019.

(143) Song, D. et al. Visualization of Dopant Oxygen Atoms in a Bi2Sr2CaCu2O8 Superconductor. *Adv. Funct. Mater.* **2019**, *29*, 1903843.

(144) Li, W.; Zhu, B.; Zhu, R.; Wang, Q.; Lu, P.; Sun, Y.; Cafolla, C.; Qi, Z.; Chen, A.; Gao, P.; Wang, H.; He, Q.; Zhang, K. H. L.; MacManus-Driscoll, J. L. Atomic-Scale Control of Electronic Structure and Ferromagnetic Insulating State in Perovskite Oxide Superlattices by Long-Range Tuning of BO 6 Octahedra. *Adv. Funct. Mater.* **2020**, *30*, 2001984.

(145) Lazić, I.; Bosch, E. G. In *Chapter Three - Analytical Review of Direct Stem Imaging Techniques for Thin Samples*; Hawkes, P. W., Ed.; Advances in Imaging and Electron Physics; Elsevier, 2017; Vol. 199; pp 75 – 184.

(146) MacLaren, I.; Wang, L.; McGrouther, D.; Craven, A. J.; McVitie, S.; Schierholz, R.; Kovács, A.; Barthel, J.; Dunin-Borkowski, R. E. On the origin of differential phase contrast

at a locally charged and globally charge-compensated domain boundary in a polar-ordered material. *Ultramicroscopy* **2015**, *154*, 57–63.

(147) Bosch, E. G. T.; Lazić, I. Analysis of Depth-Sectioning STEM for Thick Samples and 3D Imaging. *Ultramicroscopy* **2019**, *207*, 112831.

(148) Nellist, P. D.; McCallum, B. C.; Rodenburg, J. M. Resolution Beyond the 'Information Limit' in Transmission Electron Microscopy. *Nature* **1995**, *374*, 630–632.

(149) O'Leary, C. M.; Martinez, G. T.; Liberti, E.; Humphry, M. J.; Kirkland, A. I.; Nellist, P. D. Contrast transfer and noise considerations in focused-probe electron ptychography. *Ultramicroscopy* **2021**, *221*, 113189.

(150) Rodenburg, J.; McCallum, B.; Nellist, P. Experimental Tests on Double-Resolution Coherent Imaging via STEM. *Ultramicroscopy* **1993**, *48*, 304 – 314.

(151) Humphry, M. J.; Kraus, B.; Hurst, A. C.; Maiden, A. M.; Rodenburg, J. M. Ptychographic Electron Microscopy Using High-Angle Dark-Field Scattering for Sub-Nanometre Resolution Imaging. *Nat. Commun.* **2012**, *3*, 730.

(152) Maiden, A. M.; Rodenburg, J. M. An Improved Ptychographical Phase Retrieval Algorithm for Diffractive Imaging. *Ultramicroscopy* **2009**, *109*, 1256 – 1262.

(153) Rodenburg, J.; Bates, R. The Theory of Super-Resolution Electron Microscopy via Wigner-Distribution Deconvolution. *Philos. Trans. R. Soc., A* **1992**, *339*, 521–553.

(154) Pelz, P. M.; Qiu, W. X.; Bücker, R.; Kassier, G.; Miller, R. J. D. Low-Dose Cryo Electron Ptychography via Non-Convex Bayesian Optimization. *Sci. Rep.* **2017**, *7*, 9883.

(155) D'Alfonso, A. J.; Allen, L. J.; Sawada, H.; Kirkland, A. I. Dose-Dependent High-Resolution Electron Ptychography. *J. App. Phys.* **2016**, *119*, 054302.

(156) Song, B.; Ding, Z.; Allen, C. S.; Sawada, H.; Zhang, F.; Pan, X.; Warner, J.; Kirkland, A. I.; Wang, P. Hollow Electron Ptychographic Diffractive Imaging. *Phys. Rev. Lett.* **2018**, *121*, 146101.

(157) Pennycook, T. J.; Lupini, A. R.; Yang, H.; Murfitt, M. F.; Jones, L.; Nellist, P. D. Efficient Phase Contrast Imaging in STEM Using a Pixelated Detector. Part 1: Experimental Demonstration at Atomic Resolution. *Ultramicroscopy* **2015**, *151*, 160–167.

(158) Yang, H.; Jones, L.; Ryll, H.; Simson, M.; Soltau, H.; Kondo, Y.; Sagawa, R.; Banba, H.; MacLaren, I.; Nellist, P. D. 4D STEM: High Efficiency Phase Contrast Imaging Using a Fast Pixelated Detector. *J. Phys.: Conf. Ser.* **2015**, *644*, 012032.

(159) dos Reis, R.; Yang, H.; Ophus, C.; Ercius, P.; Bizarri, G.; Perrodin, D.; Shalapska, T.; Bourret, E.; Ciston, J.; Dahmen, U. Determination of the Structural Phase and Octahedral Rotation Angle in Halide Perovskites. *App. Phys. Lett.* **2018**, *112*, 071901.

(160) O'Leary, C. M.; Allen, C. S.; Huang, C.; Kim, J. S.; Liberti, E.; Nellist, P. D.; Kirkland, A. I. Phase Reconstruction Using Fast Binary 4D STEM Data. *App. Phys. Lett.* **2020**, *116*, 124101.

(161) Stevens, A.; Yang, H.; Hao, W.; Jones, L.; Ophus, C.; Nellist, P. D.; Browning, N. D. Subsampled STEM-ptychography. *App. Phys. Lett.* **2018**, *113*, 033104.

(162) Zhou, L. et al. Low-dose phase retrieval of biological specimens using cryo-electron ptychography. *Nat Commun* **2020**, *11*, 2773.

(163) Gao, S.; Wang, P.; Zhang, F.; Martinez, G. T.; Nellist, P. D.; Pan, X.; Kirkland, A. I. Electron Ptychographic Microscopy for Three-Dimensional Imaging. *Nat. Commun.* **2017**, *8*, 163.

(164) Ooe, K.; Seki, T.; Ikuhara, Y.; Shibata, N. Ultra-High Contrast STEM Imaging for Segmented/Pixelated Detectors by Maximizing the Signal-To-Noise Ratio. *Ultramicroscopy* **2020**, 113133.

(165) Kanaya, K.; Kawakatsu, H.; Ito, K.; Yotsumoto, H. Experiment on the Electron Phase Microscope. *J. App. Phys.* **1958**, *29*, 1046–1049.

(166) Danev, R.; Nagayama, K. Transmission Electron Microscopy With Zernike Phase Plate. *Ultramicroscopy* **2001**, *88*, 243 – 252.

(167) Löfgren, A.; Zeiger, P.; Kocevski, V.; Rusz, J. Influence of Nuclear Quantum Effects on Frozen Phonon Simulations of Electron Vortex Beam HAADF-STEM Images. *Ultramicroscopy* **2016**, *164*, 62 – 69.

(168) Danev, R.; Baumeister, W. Expanding the Boundaries of Cryo-Em With Phase Plates. *Curr. Opin. Struct. Biol.* **2017**, *46*, 87 – 94, Cryo electron microscopy: exciting advances in CryoEM herald a new era in structural biology Biophysical methods: behind the scenes of the cryo-EM revolution.

(169) Wang, H.-W.; Fan, X. Challenges and Opportunities in Cryo-Em With Phase Plate. *Curr. Opin. Struct. Biol.* **2019**, *58*, 175 – 182, Cryo electron microscopy Biophysical and computational methods Biophysical and computational methods - Part B.

(170) Verbeeck, J.; Tian, H.; Béché, A. A New Way of Producing Electron Vortex Probes for STEM. *Ultramicroscopy* **2012**, *113*, 83 – 87.

(171) Glaeser, R. M. Invited Review Article: Methods for imaging weak-phase objects in electron microscopy. *Review of Scientific Instruments* **2013**, *84*, 111101.

(172) Verbeeck, J.; Tian, H.; Schattschneider, P. Production and Application of Electron Vortex Beams. *Nature* **2010**, *467*, 301–304.

(173) Saitoh, K.; Hasegawa, Y.; Tanaka, N.; Uchida, M. Production of Electron Vortex Beams Carrying Large Orbital Angular Momentum Using Spiral Zone Plates. *J. Electron Microsc.* **2012**, *61*, 171–177.

(174) Harvey, T. R.; Yasin, F. S.; Chess, J. J.; Pierce, J. S.; dos Reis, R. M. S.; Özdöl, V. B.; Ercius, P.; Ciston, J.; Feng, W.; Kotov, N. A.; McMorran, B. J.; Ophus, C. Interpretable and Efficient Interferometric Contrast in Scanning Transmission Electron Microscopy With a Diffraction-Grating Beam Splitter. *Phys. Rev. App.* **2018**, *10*, 061001.

(175) Yang, H.; Ercius, P.; Nellist, P. D.; Ophus, C. Enhanced Phase Contrast Transfer Using Ptychography Combined With a Pre-Specimen Phase Plate in a Scanning Transmission Electron Microscope. *Ultramicroscopy* **2016**, *171*, 117–125.

(176) Tomita, M.; Nagatani, Y.; Murata, K.; Momose, A. Enhancement of Low-Spatial-Frequency Components by a New Phase-Contrast STEM Using a Probe Formed With an Amplitude Fresnel Zone Plate. *Ultramicroscopy* **2020**, *218*, 113089.

(177) Yu, W.; Li, S.; Zhang, Y.; Ma, W.; Sun, T.; Yuan, J.; Fu, K.; Bao, Q. Near-Infrared Photodetectors Based on $MoTe_2$/Graphene Heterostructure With High Responsivity and Flexibility. *Small* **2017**, *13*, 1700268.

(178) Schwartz, O.; Axelrod, J. J.; Campbell, S. L.; Turnbaugh, C.; Glaeser, R. M.; Müller, H. Laser phase plate for transmission electron microscopy. *Nature methods* **2019**, *16*, 1016–1020.

(179) Béché, A.; Juchtmans, R.; Verbeeck, J. Efficient Creation of Electron Vortex Beams for High Resolution STEM Imaging. *Ultramicroscopy* **2017**, *178*, 12 – 19.

(180) Candès, E. J. Compressive Sampling. *Proc. Int. Congr. Math.* **2006**,

(181) Béché, A.; Goris, B.; Freitag, B.; Verbeeck, J. Development of a Fast Electromagnetic Beam Blanker for Compressed Sensing in Scanning Transmission Electron Microscopy. *App. Phys. Lett.* **2016**, *108*, 093103.

(182) Hujsak, K.; Myers, B. D.; Roth, E.; Li, Y.; Dravid, V. P. Suppressing Electron Exposure Artifacts: An Electron Scanning Paradigm With Bayesian Machine Learning. *Microsc. Microanal.* **2016**, *22*, 778–88.

(183) Stevens, A.; Luzi, L.; Yang, H.; Kovarik, L.; Mehdi, B. L.; Liyu, A.; Gehm, M. E.; Browning, N. D. A Sub-Sampled Approach to Extremely Low-Dose STEM. *App. Phys. Lett.* **2018**, *112*, 043104.

(184) Ede, J. M.; Beanland, R. Partial Scanning Transmission Electron Microscopy With Deep Learning. *Sci. Rep.* **2020**, *10*, 8332.

(185) Trampert, P.; Bourghorbel, F.; Potocek, P.; Peemen, M.; Schlinkmann, C.; Dahmen, T.; Slusallek, P. How Should a Fixed Budget of Dwell Time Be Spent in Scanning Electron Microscopy to Optimize Image Quality? *Ultramicroscopy* **2018**, *191*, 11 – 17.

(186) Zhou, M.; Chen, H.; Ren, L.; Sapiro, G.; Carin, L.; Paisley, J. W. In *Advances in Neural Information Processing Systems 22*; Bengio, Y., Schuurmans, D., Lafferty, J. D., Williams, C. K. I., Culotta, A., Eds.; Curran Associates, Inc., 2009; pp 2295–2303.

(187) Stevens, A.; Yang, H.; Carin, L.; Arslan, I.; Browning, N. D. The Potential for Bayesian Compressive Sensing to Significantly Reduce Electron Dose in High-Resolution STEM Images. *Microscopy* **2013**, *63*, 41–51.

(188) Kovarik, L.; Stevens, A.; Liyu, A.; Browning, N. D. Implementing an Accurate and Rapid Sparse Sampling Approach for Low-Dose Atomic Resolution STEM Imaging. *App. Phys. Lett.* **2016**, *109*, 164102.

(189) Zobelli, A.; Woo, S. Y.; Tararan, A.; Tizei, L. H.; Brun, N.; Li, X.; Stéphan, O.; Kociak, M.; Tencé, M. Spatial and Spectral Dynamics in STEM Hyperspectral Imaging Using Random Scan Patterns. *Ultramicroscopy* **2020**, *212*, 112912.

(190) Potocek, P.; Trampert, P.; Peemen, M.; Schoenmakers, R.; Dahmen, T. Sparse Scanning Electron Microscopy Data Acquisition and Deep Neural Networks for Automated Segmentation in Connectomics. *Microsc. Microanal.* **2020**, *26*, 403–412.

(191) Godaliyadda, G. M. D. P.; Ye, D. H.; Uchic, M. D.; Groeber, M. A.; Buzzard, G. T.; Bouman, C. A. A Framework for Dynamic Image Sampling Based on Supervised Learning. *IEEE Transactions on Computational Imaging* **2018**, *4*, 1–16.

(192) Monier, E.; Oberlin, T.; Brun, N.; Li, X.; TencÃ©, M.; Dobigeon, N. Fast Reconstruction of Atomic-Scale STEM-EELS Images From Sparse Sampling. *Ultramicroscopy* **2020**, *215*, 112993.

(193) Spurgeon, S. R. et al. Towards Data-Driven Next-Generation Transmission Electron Microscopy. *Nat. Mater.* **2020**,

(194) Timischl, F. A Dynamic Scanning Method Based on Signal-Statistics for Scanning Electron Microscopy. *Scanning* **2014**, *36*, 317–326.

(195) Dahmen, T.; Engstler, M.; Pauly, C.; Trampert, P.; de Jonge, N.; Mücklich, F.; Slusallek, P. Feature Adaptive Sampling for Scanning Electron Microscopy. *Sci. Rep.* **2016**, *6*, 25350.

(196) Ciprari, D.; Jacob, K.; Tannenbaum, R. Characterization of Polymer Nanocomposite Interphase and Its Impact on Mechanical Properties. *Macromolecules* **2006**, *39*, 6565–6573.

(197) Midgley, P. A.; Weyland, M. 3D Electron Microscopy in the Physical Sciences: The Development of Z-Contrast and EFTEM Tomography. *Ultramicroscopy* **2003**, *96*, 413–31.

(198) Weyland, M.; Midgley, P. A. Electron Tomography. *Mater. Today* **2004**, *7*, 32–40.

(199) Kubel, C.; Voigt, A.; Schoenmakers, R.; Otten, M.; Su, D.; Lee, T. C.; Carlsson, A.; Bradley, J. Recent Advances in Electron Tomography: TEM and HAADF-STEM Tomography for Materials Science and Semiconductor Applications. *Microsc. Microanal.* **2005**, *11*, 378–400.

(200) Koster, A. J.; Ziese, U.; Verkleij, A. J.; Janssen, A. H.; de Jong, K. P. Three-Dimensional Transmission Electron Microscopy: A Novel Imaging and Characterization Technique With Nanometer Scale Resolution for Materials Science. *J. Phys. Chem. B* **2000**, *104*, 9368–9370.

(201) Bals, S.; Van Tendeloo, G.; Kisielowski, C. A New Approach for Electron Tomography: Annular Dark-Field Transmission Electron Microscopy. *Adv. Mater.* **2006**, *18*, 892–+.

(202) Xu, R.; Chen, C. C.; Wu, L.; Scott, M. C.; Theis, W.; Ophus, C.; Bartels, M.; Yang, Y.; Ramezani-Dakhel, H.; Sawaya, M. R.; Heinz, H.; Marks, L. D.; Ercius, P.; Miao, J. Three-Dimensional Coordinates of Individual Atoms in Materials Revealed by Electron Tomography. *Nat. Mater.* **2015**, *14*, 1099–103.

(203) Goris, B.; Bals, S.; Van den Broek, W.; Carbo-Argibay, E.; Gomez-Grana, S.; Liz-Marzan, L. M.; Van Tendeloo, G. Atomic-Scale Determination of Surface Facets in Gold Nanorods. *Nat. Mater.* **2012**, *11*, 930–5.

(204) Scott, M. C.; Chen, C. C.; Mecklenburg, M.; Zhu, C.; Xu, R.; Ercius, P.; Dahmen, U.; Regan, B. C.; Miao, J. W. Electron Tomography at 2.4-Angstrom Resolution. *Nature* **2012**, *483*, 444–U91.

(205) Miao, J.; Ercius, P.; Billinge, S. J. Atomic Electron Tomography: 3D Structures Without Crystals. *Science* **2016**, *353*, aaf2157.

(206) Yang, Y.; Zhou, J.; Zhu, F.; Yuan, Y.; Chang, D. J.; Kim, D. S.; Pham, M.; Rana, A.; Tian, X.; Yao, Y.; Osher, S. J.; Schmid, A. K.; Hu, L.; Ercius, P.; Miao, J. Determining the three-dimensional atomic structure of an amorphous solid. *Nature* **2021**, *592*, 60–64.

(207) Tian, X.; Kim, D. S.; Yang, S.; Ciccarino, C. J.; Gong, Y.; Yang, Y.; Yang, Y.; Duschatko, B.; Yuan, Y.; Ajayan, P. M.; Idrobo, J. C.; Narang, P.; Miao, J. Correlating the Three-Dimensional Atomic Defects and Electronic Properties of Two-Dimensional Transition Metal Dichalcogenides. *Nat. Mater.* **2020**, *19*, 867–873.

(208) Ren, D.; Ophus, C.; Chen, M.; Waller, L. A Multiple Scattering Algorithm for Three Dimensional Phase Contrast Atomic Electron Tomography. *Ultramicroscopy* **2020**, *208*, 112860.

(209) Zhou, J.; Yang, Y.; Ercius, P.; Miao, J. Atomic Electron Tomography in Three and Four Dimensions. *MRS Bull.* **2020**, *45*, 290–297.

(210) Friedrich, H.; McCartney, M. R.; Buseck, P. R. Comparison of Intensity Distributions in Tomograms From BF TEM, ADF STEM, HAADF STEM, and Calculated Tilt Series. *Ultramicroscopy* **2005**, *106*, 18–27.

(211) Goris, B.; Van den Broek, W.; Batenburg, K. J.; Mezerji, H. H.; Bals, S. Electron Tomography Based on a Total Variation Minimization Reconstruction Technique. *Ultramicroscopy* **2012**, *113*, 120–130.

(212) Stevens, A.; Yang, H.; Carin, L.; Arslan, I.; Browning, N. D. The Potential for Bayesian Compressive Sensing to Significantly Reduce Electron Dose in High-Resolution STEM Images. *Microscopy (Oxford, U. K.)* **2014**, *63*, 41–51.

(213) Wang, G.; Garcia, D.; Liu, Y.; de Jeu, R.; Johannes Dolman, A. A Three-Dimensional Gap Filling Method for Large Geophysical Datasets: Application to Global Satellite Soil Moisture Observations. *Environ. Modell. Software* **2012**, *30*, 139–142.

(214) Zhang, J.; Zhao, D.; Gao, W. Group-Based Sparse Representation for Image Restoration. *IEEE Trans. Image Process* **2014**, *23*, 3336–51.

(215) Leary, R.; Saghi, Z.; Midgley, P. A.; Holland, D. J. Compressed Sensing Electron Tomography. *Ultramicroscopy* **2013**, *131*, 70–91.

(216) Saghi, Z.; Holland, D. J.; Leary, R.; Falqui, A.; Bertoni, G.; Sederman, A. J.; Gladden, L. F.; Midgley, P. A. Three-Dimensional Morphology of Iron Oxide Nanoparticles With Reactive Concave Surfaces. A Compressed Sensing-Electron Tomography (CS-ET) Approach. *Nano Lett.* **2011**, *11*, 4666–73.

(217) Thomas, J. M.; Leary, R.; Midgley, P. A.; Holland, D. J. A New Approach to the Investigation of Nanoparticles: Electron Tomography With Compressed Sensing. *J. Colloid Interface Sci.* **2013**, *392*, 7–14.

(218) Iancu, C. V.; Tivol, W. F.; Schooler, J. B.; Dias, D. P.; Henderson, G. P.; Murphy, G. E.; Wright, E. R.; Li, Z.; Yu, Z.; Briegel, A.; Gan, L.; He, Y.; Jensen, G. J. Electron Cryotomography Sample Preparation Using the Vitrobot. *Nat. Protoc.* **2006**, *1*, 2813—2819.

(219) Lucic, V.; Rigort, A.; Baumeister, W. Cryo-Electron Tomography: The Challenge of Doing Structural Biology in Situ. *J. Cell. Biol.* **2013**, *202*, 407–19.

(220) Li, Y.; Hujsak, K. A.; Backman, V.; Dravid, V. P. Inpainting Assisted Controlled Rotation Tomography (CORT). *Microsc. Microanal.* **2018**, *24*, 502–503.

(221) Brown, H. G.; Pelz, P. M.; Hsu, S.-L.; Zhang, Z.; Ramesh, R.; Inzani, K.; Sheridan, E.; Griffin, S. M.; Findlay, S. D.; Allen, L. J.; Scott, M. C.; Ophus, C.; Ciston, J. A Three-Dimensional Reconstruction Algorithm for Scanning Transmission Electron Microscopy Data From Thick Samples. 2020.

(222) Gao, S.; Wang, P.; Zhang, F.; Martinez, G. T.; Nellist, P. D.; Pan, X.; Kirkland, A. I. Electron Ptychographic Microscopy for Three-Dimensional Imaging. *Nat. Commun.* **2017**, *8*, 163.

(223) Gao, S.; Ding, Z.; Pan, X.; Kirkland, A. I.; Wang, P. 3D Electron Ptychography. *Microsc. Microanal.* **2019**, *25*, 1802–1803.

(224) Cheng, Y.; Grigorieff, N.; Penczek, P. A.; Walz, T. A primer to single-particle cryo-electron microscopy. *Cell* **2015**, *161*, 438–449.

(225) Cheng, Y. Single-Particle Cryo-EM at Crystallographic Resolution. *Cell* **2015**, *161*, 450–457.

(226) Frank, J.; Goldfarb, W.; Eisenberg, D.; Baker, T. S. Reconstruction of glutamine synthetase using computer averaging. *Ultramicroscopy* **1978**, *3*, 283–90.

(227) FRANK, J. *Single-Particle Cryo-Electron Microscopy*; pp 69–72.

(228) Lyumkis, D. Challenges and Opportunities in Cryo-Em Single-Particle Analysis. *J. Bio. Chem.* **2019**, *294*, 5181–5197.

(229) Glaeser, R. M. How Good Can Single-Particle Cryo-Em Become? What Remains Before It Approaches Its Physical Limits? *Annu. Rev. Biophys.* **2019**, *48*, 45–61, PMID: 30786229.

(230) Pan, Y.-H.; Sader, K.; Powell, J. J.; Bleloch, A.; Gass, M.; Trinick, J.; Warley, A.; Li, A.; Brydson, R.; Brown, A. 3D Morphology of the Human Hepatic Ferritin Mineral Core: New Evidence for a Subunit Structure Revealed by Single Particle Analysis of HAADF-STEM Images. *J. Struct. Biol.* **2009**, *166*, 22 – 31.

(231) Wang, Y.-C.; Slater, T. J. A.; Leteba, G. M.; Roseman, A. M.; Race, C. P.; Young, N. P.; Kirkland, A. I.; Lang, C. I.; Haigh, S. J. Imaging Three-Dimensional Elemental Inhomogeneity in Pt–Ni Nanoparticles Using Spectroscopic Single Particle Reconstruction. *Nano Lett.* **2019**, *19*, 732–738.

(232) Li, Y.; Roth, E.; Agrawal, V.; Eshein, A.; Fredrick, J.; Almassalha, L.; Shim, A.; Bleher, R.; Dravid, V. P.; Backman, V. Quantifying Three-dimensional Chromatin Organization Utilizing Scanning Transmission Electron Microscopy: ChromSTEM. *bioRxiv* **2019**,

(233) Jung, H. J.; Kim, D.; Kim, S.; Park, J.; Dravid, V. P.; Shin, B. Stability of Halide Perovskite Solar Cell Devices: In Situ Observation of Oxygen Diffusion Under Biasing. *Adv. Mater.* **2018**, *30*, e1802769.

(234) Sinclair, R.; Itoh, T.; Chin, R. In Situ TEM Studies of Metal-Carbon Reactions. *Microsc. Microanal.* **2002**, *8*, 288–304.

(235) Ge, D.; Domnich, V.; Juliano, T.; Stach, E. A.; Gogotsi, Y. Structural Damage in Boron Carbide Under Contact Loading. *Acta Mater.* **2004**, *52*, 3921–3927.

(236) Murthy, A. A.; Stanev, T. K.; Dos Reis, R.; Hao, S.; Wolverton, C.; Stern, N. P.; Dravid, V. P. Direct Visualization of Electric-Field-Induced Structural Dynamics in Monolayer Transition Metal Dichalcogenides. *ACS Nano* **2020**, *14*, 1569–1576.

(237) Kim, S.; Jung, H. J.; Kim, J. C.; Lee, K. S.; Park, S. S.; Dravid, V. P.; He, K.; Jeong, H. Y. In Situ Observation of Resistive Switching in an Asymmetric Graphene Oxide Bilayer Structure. *ACS Nano* **2018**, *12*, 7335–7342.

(238) de Jonge, N.; Houben, L.; Dunin-Borkowski, R. E.; Ross, F. M. Resolution and Aberration Correction in Liquid Cell Transmission Electron Microscopy. *Nat. Rev. Mater.* **2019**, *4*, 61–78.

(239) He, K.; Shokuhfar, T.; Shahbazian-Yassar, R. Imaging of Soft Materials Using in Situ Liquid-Cell Transmission Electron Microscopy. *J. Phys. Condens. Matter* **2019**, *31*, 103001.

(240) Liu, W. J.; Shi, Q.; Qu, Q. T.; Gao, T.; Zhu, G. B.; Shao, J.; Zheng, H. H. Improved Li-Ion Diffusion and Stability of a LiNi0.5Mn1.5O4 Cathode Through in Situ Co-Doping With Dual-Metal Cations and Incorporation of a Superionic Conductor. *Journal of Materials Chemistry A* **2017**, *5*, 145–154.

(241) Nie, A.; Gan, L. Y.; Cheng, Y.; Li, Q.; Yuan, Y.; Mashayek, F.; Wang, H.; Klie, R.; Schwingenschlogl, U.; Shahbazian-Yassar, R. Twin Boundary-Assisted Lithium Ion Transport. *Nano Lett.* **2015**, *15*, 610–5.

(242) Cooper, D.; Baeumer, C.; Bernier, N.; Marchewka, A.; La Torre, C.; Dunin-Borkowski, R. E.; Menzel, S.; Waser, R.; Dittmann, R. Anomalous Resistance Hysteresis in Oxide ReRAM: Oxygen Evolution and Reincorporation Revealed by in Situ TEM. *Adv. Mater.* **2017**, *29*, 1700212.

(243) Azizi, A.; Zou, X.; Ercius, P.; Zhang, Z.; Elias, A. L.; Perea-Lopez, N.; Stone, G.; Terrones, M.; Yakobson, B. I.; Alem, N. Dislocation Motion and Grain Boundary Migration in Two-Dimensional Tungsten Disulphide. *Nat. Commun.* **2014**, *5*, 4867.

(244) Park, J.; Elmlund, H.; Ercius, P.; Yuk, J. M.; Limmer, D. T.; Chen, Q.; Kim, K.; Han, S. H.; Weitz, D. A.; Zettl, A.; Alivisatos, A. P. Nanoparticle Imaging. 3D Structure of Individual Nanocrystals in Solution by Electron Microscopy. *Science* **2015**, *349*, 290–5.

(245) Li, X.; Mooney, P.; Zheng, S.; Booth, C. R.; Braunfeld, M. B.; Gubbens, S.; Agard, D. A.; Cheng, Y. Electron Counting and Beam-Induced Motion Correction Enable Near-Atomic-Resolution Single-Particle Cryo-Em. *Nat. Methods* **2013**, *10*, 584–90.

(246) Jones, L.; Varambhia, A.; Beanland, R.; Kepaptsoglou, D.; Griffiths, I.; Ishizuka, A.; Azough, F.; Freer, R.; Ishizuka, K.; Cherns, D.; Ramasse, Q. M.; Lozano-Perez, S.; Nellist, P. D. Managing Dose-, Damage- And Data-Rates in Multi-Frame Spectrum-Imaging. *Microscopy* **2018**, *67*, i98–i113.

(247) Murthy, A. A.; Stanev, T. K.; Ribet, S. M.; Liu, P.; Watanabe, K.; Taniguchi, T.; Stern, N. P.; dos Reis, R.; Dravid, V. P. Spatial Mapping of Electrostatics and Dynamics across 2D Heterostructures. 2020.

(248) Meredig, B. Five High-Impact Research Areas in Machine Learning for Materials Science. *Chem. Mater.* **2019**, *31*, 9579–9581.

(249) Sadre, R.; Ophus, C.; Butko, A.; Weber, G. H. Deep Learning Segmentation of Complex Features in Atomic-Resolution Phase Contrast Transmission Electron Microscopy Images. *arXiv preprint arXiv:2012.05322* **2020**,

(250) Lee, C.-H.; Khan, A.; Luo, D.; Santos, T. P.; Shi, C.; Janicek, B. E.; Kang, S.; Zhu, W.; Sobh, N. A.; Schleife, A.; Clark, B. K.; Huang, P. Y. Deep Learning Enabled Strain Mapping of Single-Atom Defects in Two-Dimensional Transition Metal Dichalcogenides With Sub-Picometer Precision. *Nano Lett.* **2020**, *20*, 3369–3377, PMID: 32243178.

(251) Zhang, C.; Feng, J.; DaCosta, L. R.; Voyles, P. Atomic resolution convergent beam electron diffraction analysis using convolutional neural networks. *Ultramicroscopy* **2020**, *210*, 112921.

(252) Lee, P.; West, J. D.; Howe, B. Viziometrics: Analyzing Visual Information in the Scientific Literature. *IEEE Trans. Big Data* **2018**, *4*, 117–129.

(253) Arganda-Carreras, I.; Kaynig, V.; Rueden, C.; Eliceiri, K. W.; Schindelin, J.; Cardona, A.; Sebastian Seung, H. Trainable Weka Segmentation: a machine learning tool for microscopy pixel classification. *Bioinformatics* **2017**, *33*, 2424–2426.

(254) Ziatdinov, M.; Dyck, O.; Maksov, A.; Li, X.; Sang, X.; Xiao, K.; Unocic, R. R.; Vasudevan, R.; Jesse, S.; Kalinin, S. V. Deep Learning of Atomically Resolved Scanning Transmission Electron Microscopy Images: Chemical Identification and Tracking Local Transformations. *ACS Nano* **2017**, *11*, 12742–12752, PMID: 29215876.

(255) Bruno, I.; Gražulis, S.; Helliwell, J. R.; Kabekkodu, S. N.; McMahon, B.; Westbrook, J. Crystallography and Databases. *Data Sci. J.* **2017**, *16*.

(256) Nord, M.; Webster, R. W. H.; Paton, K. A.; McVitie, S.; McGrouther, D.; MacLaren, I.; Paterson, G. W. Fast Pixelated Detectors in Scanning Transmission Electron Microscopy. Part I: Data Acquisition, Live Processing, and Storage. *Microsc. Microanal.* **2020**, *26*, 653–666.

(257) Pelz, P. M.; Johnson, I.; Ophus, C.; Ercius, P.; Scott, M. C. Real-time interactive 4D-STEM phase-contrast imaging from electron event representation data. **2021**,

(258) Wilkinson, M. D. et al. The FAIR Guiding Principles for Scientific Data Management and Stewardship. *Sci. Data* **2016**, *3*, 160018.

(259) Taillon, J. A.; Bina, T. F.; Plante, R. L.; Newrock, M. W.; Greene, G. R.; Lau, J. W. NexusLIMS: A Laboratory Information Management System for Shared-Use Electron Microscopy Facilities. *Microscopy and Microanalysis* **2021**, 1–17.

(260) Andreev, A.; Koo, D. E. Practical guide to storage of large amounts of microscopy data. *Microscopy Today* **2020**, *28*, 42–45.

(261) Savitzky, B. H. et al. Py4DSTEM: A Software Package for Multimodal Analysis of Four-Dimensional Scanning Transmission Electron Microscopy Datasets. 2020.

(262) Johnstone, D. N. et al. pyxem/pyxem: pyxem 0.10.1. 2020; `https://doi.org/10.5281/zenodo.3667613`.

(263) Clausen, A. et al. LiberTEM/LiberTEM: 0.5.1. 2020; `https://doi.org/10.5281/zenodo.3982290`.

(264) Somnath, S.; CompPhysChris,; ramav87,; Laanait, N.; Giridharagopal, R.; str eat,; Carlo,; anugrah saxena,; Dyck, O.; Kong, J.; Liambcollins,; Lopez-Guerra, E. A.; Nord, M.; Tee, K.; Agar, J. C. pycroscopy/pycroscopy: 0.60.7-beta. 2020; `https://doi.org/10.5281/zenodo.4008763`.

(265) Nord, M. pixstem. 2020; `https://pixstem.org/`.

(266) de la Peña, F. et al. hyperspy/hyperspy: Release v1.6.1. 2020; `https://doi.org/10.5281/zenodo.4294676`.

Acknowledgement

This material is based upon work supported by the National Science Foundation under Grant No. DMR-1929356. This work made use of the Electron Probe Instrumentation Center (EPIC) and BioCryo facilities of Northwestern University's NU*ANCE* Center, which has received support from the Soft and Hybrid Nanotechnology Experimental (SHyNE) Resource (NSF ECCS-2025633), the IIN, and Northwestern's MRSEC program (NSF DMR-1720139). A.A.M. gratefully acknowledges support from the Ryan Fellowship and the IIN at Northwestern University. This work was supported by Air Force Research Laboratory grant FA8650-15-2-5518, and partially supported by Air Force Office of Scientific Research award number FA9550-17-1-0348 and Army Research Office MURI grant W911NF1810200. Research reported in this publication was supported in part by instrumentation provided by the Office of The Director, National Institutes of Health of the National Institutes of Health under Award Number S10OD026871. The content is solely the responsibility of the authors and does not necessarily represent the official views of the National Institutes of Health. This research was supported in part through the computational resources and staff contributions provided for the Quest high performance computing facility at Northwestern University which is jointly supported by the Office of the Provost, the Office for Research, and Northwestern University Information Technology.

Supplementary Information

Imaging Hard-Soft Interfaces in Low-Dimensional Nanocomposites with Scanning/Transmission Electron Microscopy

Stephanie M. Ribet[a,1], Akshay A. Murthy[a,b,d,1], Eric W. Roth[c], Roberto dos Reis[a,c], Vinayak P. Dravid[a,b,c,*]

[1] These authors contributed equally

[a] Department of Materials Science and Engineering, Northwestern University, Evanston, IL, USA

[b] International Institute of Nanotechnology, Northwestern University, Evanston, IL, USA

[c] The NU*ANCE* Center, Northwestern University, Evanston, IL, USA

[d] Now at Fermi National Accelerator Laboratory, Batavia, IL, USA

[*] Corresponding Author:

Vinayak P. Dravid: v-dravid@northwestern.edu

S1 Methods

S1.1 Sample Preparation

For the materials analyzed in this paper, Au, Fe_3O_4, and SiO_2 nanoparticles in aqueous suspensions were pipetted into a BEEM capsule and dried in an oven at 60°C overnight. Approximately 20μL of EMBed812 epoxy resin was placed at the bottom of the capsule and mixed with the dry nanoparticles prior to filling the rest of the capsule with resin and curing at 60°C for 48 hours. Ultrathin 60nm sections of the embedded samples were cut with a 35° diamond knife (Diatome) on a Leica UC7 ultramicrotome.

S1.2 Image Acquisition

Scanning Transmission Electron Micro images were acquired using the JEOL ARM 300F (operated at 300 kV) and ADF $>$ 100 mrad.

S1.3 4D STEM Acquisition

4D STEM datasets were collected using Gatan OneView camera and K3 IS installed, respectively, on a JEOL ARM 200CF operated at 200 kV with convergence angle of 6.9mrad and a JEOL Grand ARM 300F operated at 300 kV with convergence angle of 30mrad. For Figure 3 dataset of size 64x50x512x512 at a frame rate of 10fps (0.1s per diffraction) simultaneously collected with EDS dataset was acquired using OneView detector. For Figure 4, a dataset of 100x100x1024x1024 at a frame rate of 285 fps (0.0035s per diffraction) was acquired using K3 IS detector in counting mode.

S1.4 STEM Simulations

Custom MatLab codes were used to perform multislice simulations following the methods laid out by Kirkland.[109] These simulations used the described ADF imaging parameters with eight frozen phonon configurations. The simulation in Figure 5 was performed on an approximately 1nm thin sample. The thickness of this sample is artificially thin to meet the weak phase object approximation. 30 mrad STEM probes simulated at 300kV with no probe aberrations were spaced by 0.4 Å. The electron dose was modified by combining the image matrix and a shot noise matrix following a Poisson distribution with different ratios. For the adaptive sampling images, a higher dose image of the gold region was stitched together with a lower dose image of the carbon matrix followed by a Gaussian filter.

S1.5 Integrated DPC and Differentiated DPC

Integrated DPC was carried out following the methods outlined by Lazić et al.[134] The DPC_x and DPC_y images were first combined to form a vector image. The integrated signal of the Fourier transform of the vector image was then calculated. Finally, an inverse Fourier transform of the resultant calculation was taken to construct the iDPC or phase image.

Differentiated DPC images were constructed by similarly following the methods outlined by Lazić et al. and taking the divergence of the vector images.[134]

S1.6 Ptychography

Electron ptychography reconstruction was conducted using the single sideband (SSB) method within the py4DSTEM Python package.[261]

S1.7 Phase Plate STEM

For the purposes of this simulation a $\mathrm{MoTe_2}$/graphene heterostructure was studied. A 4D STEM multislice approach was applied with a 35 mrad probe simulated at 300kV modified using a Fresnel aperture with rings of alternating intensity of i and 1. Probe positions were 0.5 Å apart. Final images were reconstructed by integrating rings of the same phase of the pre-specimen probe. CTF was calculated using the method as described by Ophus et al..[61]

Graphical TOC Entry